FAIRCHILD
SPACE

IN-71-CR
8-79

ON THE NATURE OF THE FRAGMENT ENVIRONMENT CREATED BY THE RANGE DESTRUCTION OR RANDOM FAILURE OF SOLID ROCKET MOTOR CASINGS

M. ECK
M. MUKUNDA

JULY, 1988

FSC-ESD-217-88-426

FAIRCHILD SPACE • 20301 CENTURY BOULEVARD • GERMANTOWN, MARYLAND 20874

FSC–ESD–217–88–426

ON THE NATURE OF THE FRAGMENT ENVIRONMENT CREATED BY THE RANGE DESTRUCTION OR RANDOM FAILURE OF SOLID ROCKET MOTOR CASINGS

INTERIM REPORT, JPL CONTRACT 957524

M. ECK
M. MUKUNDA

JULY, 1988

This report was prepared for the Jet Propulsion Laboratory, California Institute of Technology, sponsored by the National Aeronautics and Space Administration.

FAIRCHILD
S P A C E

TABLE OF CONTENTS

LIST OF FIGURES

LIST OF TABLES

I. INTRODUCTION AND SUMMARY

The Galileo spacecraft is a deep space probe. All deep space probes are powered by Radioisotope Thermoelectric Generators (RTGs). These devices produce power by converting the heat generated by the decay of the radioactive isotope Pu-238 into electricity. Packaging this radioisotope to ensure that its use presents no hazard to the general public is a principal power system design concern. Considerable analytical and experimental efforts are expended to review the safety of any radioisotope powered spacecraft. This effort is documented in a Final Safety Analysis Report (FSAR) for the mission. Launch approval requires the acceptance of the adequacy of the FSAR by the Presidential Science Advisory Council.

The Challenger (STS-51L) accident demonstrated that fragmentation of the STS Solid Rocket Motors (SRM) presented a potential impact hazard which had not been considered in the then current FSAR. A number of analysts immediately began to consider the possible consequences of the impact of a large SRM fragment on the Galileo GPHS-RTG. Fairchild Space Company personnel first became involved in predicting the response of the GPHS-RTG to explosion and explosion driven shrapnel environments in June 1984. Because of this experience, the authors were asked, in May 1986, to participate in the 51L explosion working group activity then being initiated by JPL and KSC. The activity of this group involved assessing the yield of the 51L external tank explosion if any; predicting the environment produced by a confined by missile (CMB) explosion of a Centaur G' had it been on board the 51L, and predicting the velocity of the SRM fragments which were generated by the range destruct action initiated at a mission elapsed time (MET) of 110 seconds. This latter effort was subsequently enlarged to include all SRM fragment information required for the Shuttle Data Book. The first two subjects listed above are covered by other topical reports. The contents of this report are confined to predictions of the fragment velocities and azimuths resulting from an STS-SRM range destruct, or random failure occurring at any time during the 120 seconds of SRM burn.

Calculational methods were devised to predict the velocity of the 51L SRM fragments produced by the 110 sec MET range destruct. These methods were exercised and calibrated against the results determined by photographic interpretation of the PIGOR film record[5] of the 51L event. Good agreement was obtained between the analytical predictions and the experimental observations, and these results were first presented to the Shuttle Data Book working group in September 1986. A circumstance of nature (the failure of the Titan 34D-9 SRM in April 1986) provided a datum against which to check the analytical models at early MET (10 sec). Analytical models of the 34D were prepared and it was found that the methods which had been used for performing late MET predictions underpredicted early MET SRM fragment velocities by a factor of two.

After study of the 34D-9 films and a review of the analytical methods used, it became obvious that allowances for effects of casing-grain debonding must be made when predicting early MET failures. A method for interacting the complex high pressure gas flow field with the debonded casing and grain was devised. This method was first presented in a briefing at JSC in February 1987; it was developed, refined, and implemented in the period between September 1987 and January 1988. The effort described in this report constitutes the analytical basis for the fragment velocities, velocity distributions, and azimuths which are presented in the Shuttle Data Book.

The fragment-flow-field interaction pattern shown in Figure 1 is typical of the results obtained using the described techniques. This particular model is of the forward cylinder of an aft-center segment of an STS-SRM undergoing random failure at an altitude of 36,600 m. Point calculations were performed at 10, 84, and 110 sec MET for both range destruct and random failure cases. The detailed results of these calculations were transmitted to JPL and GE on magnetic tape. A hard copy of those results is presented in Appendix A in some, but not all, copies of this report.

A comparison of predicted and observed results for a variety of mission failure scenarios is shown in Table 1. The predictions made using the methods discussed in this report were in good agreement with observations made by others. It should be noted that, with one

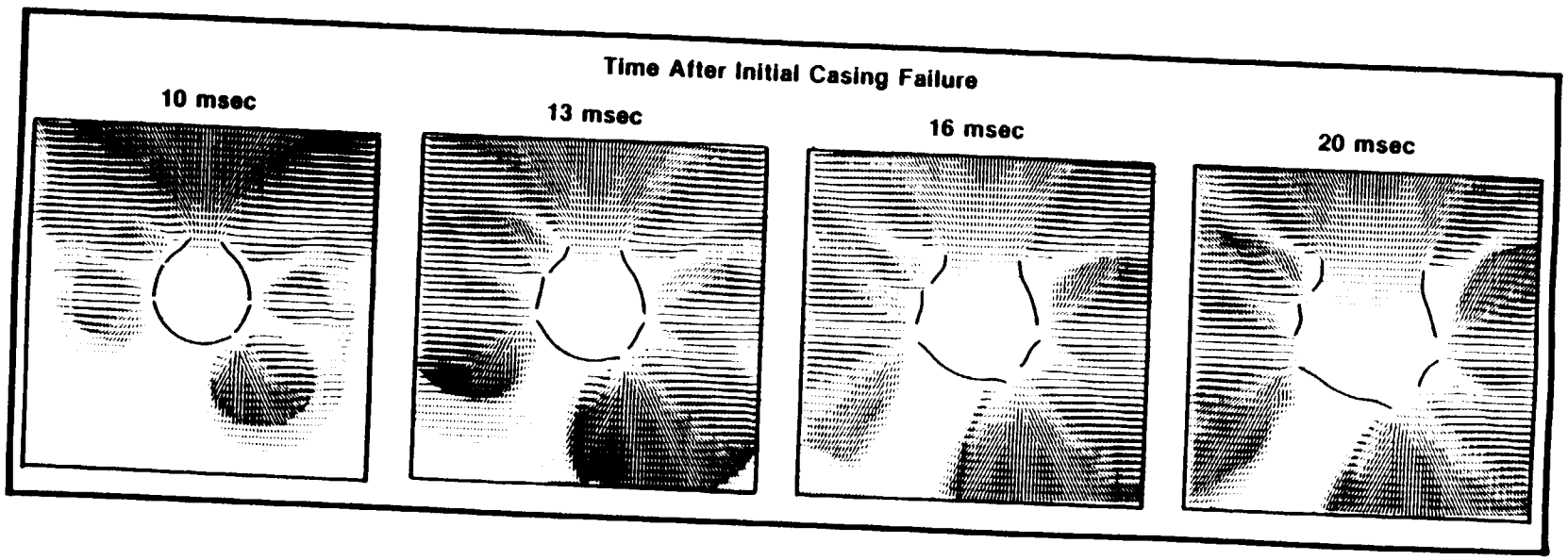

Figure 1. Flow Field Developing Around a Randomly Failed STS Forwarded Cylinder With Fragmentation Occurring 5 msec After Initial Casing Failure (110 Seconds MET)

Table 1. Summary of the Predicted and Observed Fragmentation Response of Several Vehicle Elements to a Number of Internal Pressure Environments

Booster / Event	Vessel Pressure at Time of Initial Failure	Failure MET	Fragmentation Time[a]	Predicted Range of Fragment Velocities[e][f]	Observed Range of Fragment Velocities	Predicted Range of Fragment Rotation Rates[e]	Observed Range of Fragment Rotation Rates
	Bar	sec	msec	m/s	m/s	Hz	Hz
34D-9 Range Destruct	54.5	10.	0-20	17-104	15-106[c]	8-12	5-12
34D-9 Random[b] Failure	54.5	10.	0-20[d]	15-111	15-114[c]	8-12	5-12
STS Range Destruct	60.	10.	0-20	2-108	—	1-12	—
STS Random Failure	60.	10.	0-20	2-115	—	1-12	—
STS Range Destruct	41.4	84.	0-20	30-104	—	1-11	—
STS Random Failure	41.4	84.	0-20	53-123	—	1-12	—
STS-51L Range Destruct (Fwd. Cyl.)	31.0	110.	0-20	6-162	15-198	0-11	3-17
STS-51L Range Destruct (Aft. Cyl)	31.0	110.	0-20	19.8-226.	15-198	1-19	3-17
STS Random Failure (Fwd. Cyl.)	31.	110.	0-20	3.-169.	—	0-12	—

[a]Time after initial grain fragmentation at which casing fragments are generated. The latest time at which shell stresses can be supported by casing-materials' strength.

[b]A 320 m/s propagation rate is used to communicate the crack from segment to segment.

[c]Based on analyses of range data performed by Jaffe[3] using a six degree of freedom code.

[d]Instantaneous fragmentation is assumed in the randomly failed segment followed by subsequent segment casing failure up to 20 msec after the arrival of a propagating (320 m/s) crack at the relevant segment boundary.

[e]Ranges vary from early-fragmentation-large-fragments to late-fragmentation time-small fragments adjacent to the initial casing-crack free-surface.

[f]Note that all random failure generated fragment velocity ranges are for the fragmented cylinder. The cylinders adjacent to this cylinder will have serially decreasing maximum fragment velocities. This decrease may be more than a factor of two when the randomly failed cylinder is at a stack extreme. At low crack propagation rates the extreme cylinder may not fragment.

exception, the authors made their analytical predictions before they knew the corresponding experimental results. This was purposely done to provide a single-blind experiment. A complete explanation of the analytical methods developed and their boundary assumptions is presented in the following chapter.

Shortly after this report was issued in draft form, analysts from the Naval Surface Warefare Center (NSWC) presented the results of their analytical studies of potential SRM fragment velocities. These studies resulted in their prediction of higher fragment velocities at early MET and lower fragment velocities at late MET than are presented in the report at hand. NASA management convoked an ad hoc Committee chaired by Dr. Franklin Moore to study the analytical methods and boundary condition assumptions used by both sets of investigators and to reconcile the different velocity predictions if possible. A large amount of new material was developed to answer questions raised by the Moore Committee. This material, in all cases, confirmed the efficacy of the methods used. It does not, however, provide a detailed fragmentation mechanism which could be developed from first principles. Subsequent analyses have shown that the fragmentation mechanism requires detailed modeling of the SRM cylinder joints before it presents itself.

The material presented to the Moore Committee in defense of the methods used in the study at hand is included in an Epilogue to this document. Detailed three-dimensional calculations which identified the SRM fragmentation mechanism have been presented in subsequent reports by the authors. The findings of the Moore Committee are a matter of public record.

II. TECHNICAL DISCUSSION

The initial approach taken to predicting the SRM failure-generated fragment environment was somewhat conventional. The modeling methods involved defining a gas flow field in an Eulerian coordinate system, defining an SRM casing structure in a Lagrangian coordinate system and coupling the two coordinate systems. The flow field definition required knowledge of the vessel internal pressure at the time of failure and the physical properties of the expanding gas. The shell modeling required knowledge of the materials of construction of the vessel and its detailed geometry. All fragment velocity calculations were performed in two-dimensions using x-y translational symmetry arguments. The flow fields and the chamber longitudinal pressure distributions for random failure cases were calculated in two-dimensions using an axisymmetrical argument. The Physics-International-developed finite-difference continuum-mechanics code PISCES[11] was used to mechanize the computational process. It soon became apparent that while the methods originally employed were computationally sound, the assumption that chamber pressure acted only on the inner surface of the grain was not sound. Further, it was clear that different failure mechanisms were at work when large amounts of grain were present and when they were not (early MET and late MET).

Significant differences were found to exist between early MET SRM failure when there were substantial amounts of unburned PBAN grain remaining and later MET when the grain was less than about 15 cm thick. In addition, it was clear that there were significant differences in the time-history of the chamber longitudinal pressure gradient in SRM failures caused by random and range destruct actions.

The material in the following sections describes the methods used to predict fragment velocities, azimuths and rotation rate generated by:

A. SRM Range Destruct Actions

B. SRM Random Failures

Fragment environments generated by range destruct actions and random failures occurring at 10, 84 and 110 sec MET were predicted by applying the methods presented in the following sections. More detailed results of these predictions are presented in Appendix A.

A. SRM Fragmentation Resulting From Range Destruct Actions

Initial calculations were performed to determine if the available codes and models could be used to make approximately correct predictions of fragment velocities resulting from range destruct actions. These calculations were also used in an attempt to define mechanistic SRM casing and grain failure models. Even when traveling stress waves generated by the linear shaped charge (LSC) were included, the predicted stress levels never exceeded the yield strength of the D6A steel used in the SRM casings. The possibility of three dimensional bending effects was considered but Euler calculations showed very rapid decreases in chamber pressure with time. It was not clear how bending waves (which travel at about 20 percent of the sound speed) could affect the largely two dimensional local casing bending in the 20-40 msec available. It rapidly became clear that the time at which the SRM casing fragmented was controlled by statistical phenomena such as the location of crack nucleation sites, complex bending wave interactions, and the notch sensitivity of the casing steel. Since no micro-failure-mechanism could be identified, it was concluded that the efficacy of any analytical model must be evaluated on a macro scale. The only reasonable way to accomplish this was to compare predicted results to observations made of actual SRM failures. It was reasoned that the ground location of the fragments resulting from the Titan 34D-9 failure would give reliable witness to the time after initial casing failure at which these fragments were generated. Combining these early MET range data with late MET STS-51L photo data would provide a reasonable data base against which an analytical model could be calibrated.

The approximate time of casing fragmentation was important to the safety analysis because this time has a first order effect on fragment azimuth and a second order effect on fragment velocity. Fragment-RTG hit probability, therefore, becomes a strong function of fragmentation time. It was known that the circumferential shock transit time of the 34D-9

casing was approximately 2.5 msec. It was unlikely therefore, that fragmentation could occur less than 2.5 msec after the formation of the first casing-crack free-surface. Crack propagation in the PBAN fuel is significantly slower than in steel and flame propagation is even slower. Therefore, it was reasoned that very little energy, beyond that which was stored in the hot chamber gases, would be added during a SRM failure. Sensitivity studies were carried out using various assumed energy addition rates and this notion was found correct. It is true that contained, local, hot spots caused by inhibitor debonding can cause random failures of SRM casings. But it must be remembered that the locally high energy involved in these events is still small in relation to the total energy stored in the hot chamber gases.

A number of sensitivity calculations were performed once the above ground rules were established. A summary of the sensitivity calculation predictions for SRM fragments generated 20 msec after range destruct actions were initiated is presented in Figure 2. The chamber-pressure-time-histories resulting from SRM failures at a number of mission elapsed times are presented in Figure 3. Note that zero time in all SRM fragmentation scenarios is defined as the time at which the first crack completely traverses the grain. This should not be confused with LSC initiation time or first casing-crack free-surface formation time which may be up to 15 msec earlier. This distinction is important because the mass of chamber gas does not begin to decrease until the first flow-passage through the grain is generated. Since there is no loss of chamber gas mass, the chamber pressure can only decrease by increasing the grain inner diameter. This has important pressure-time-history implications, as will be shown later.

The two-dimensional Eulerian-Lagrangian-coupled calculations shown in Figure 2 tied the rate of chamber pressure decrease to the movement of the SRM casing. The casing movement was assumed to be a "clamshell" opening about a hinge point located 180 degrees from the initial casing fracture. Additional calculations were performed which allowed arbitrary geometric fragmentation of the casing. Although arbitrary, the selection of these fracture locations was based on first hand inspection of the fragments from 51L and a review of the photographic reconstruction records of 34D-9. The results of these calculations are presented in Figure 4. These initial calculations were based on the assumption that the chamber pressure

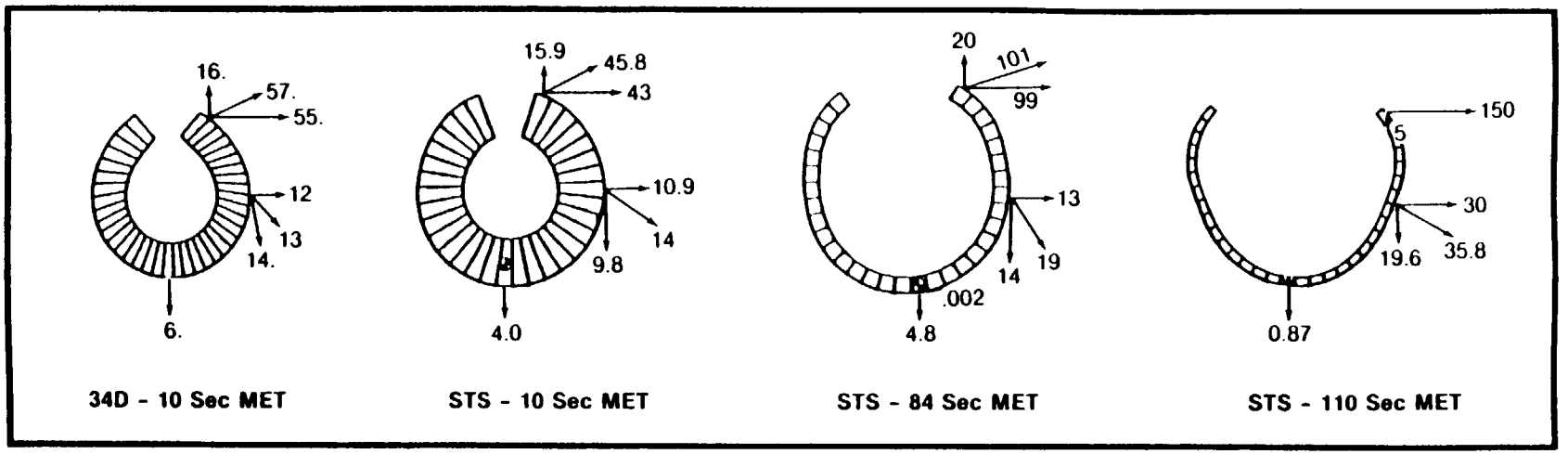

Figure 2. SRM Fragment Geometries and Velocities (m/s) 20 msec After a Range Destruct Action at Three Mission Elapsed Times (MET) Assuming No Casing-Grain Debonding

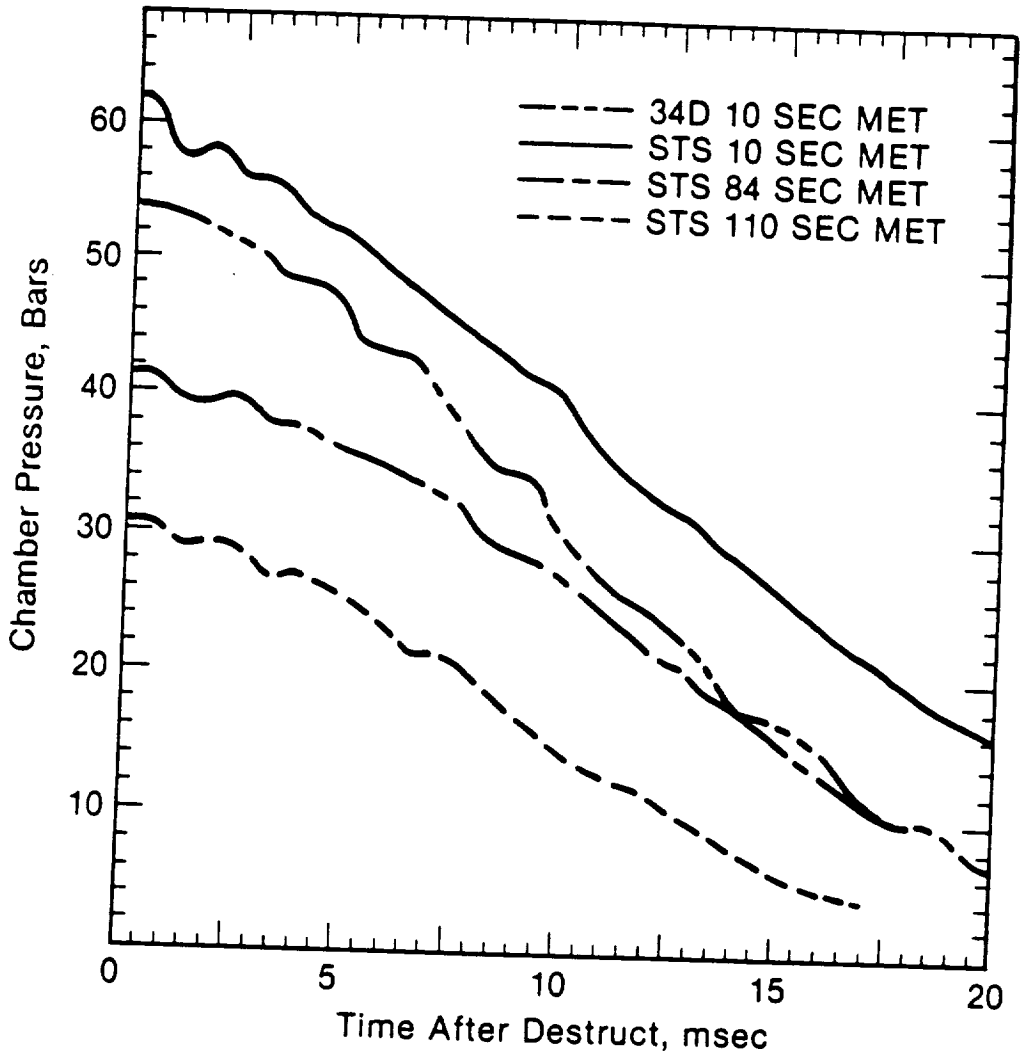

Figure 3. **Comparison of the Effects of MET and Geometry on SRM Chamber-Pressure Decrease Following a Range Destruct Action**

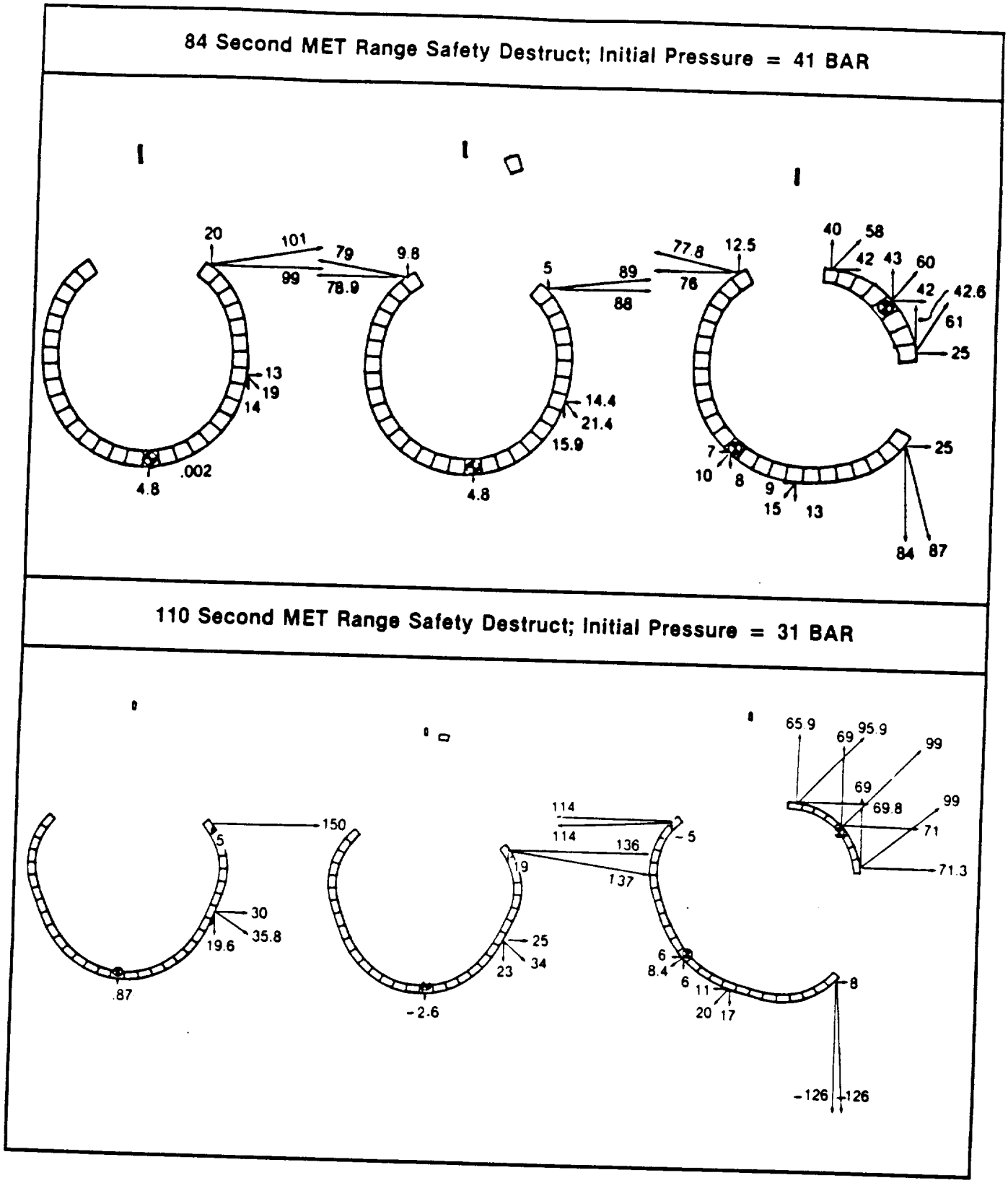

Figure 4. SRM Fragment Geometries and Velocities (m/s) 20 msec After a Range Destruction at 84 and 110 Seconds MET

acted only on the inside diameter of the PBAN grain and accelerated the chamber casing and grain as a single body.

The forces acting on the PBAN grain shown in Figure 2 and Figure 4 were predicted using a 5,000 zone Eulerian model of the gas flow field which had a minimum cell size of 15 cm x 30 cm and was further defined by the nature of the PBAN gas and its current pressure. The rate at which the SRM casings deformed was controlled by the strength of the Lagrangian modeled casings and grains, and their inertias. Component inertia was by far the controlling effect. Initial predictions made for early MET were found to be in error because they did not consider the flow field which resulted if PBAN-casing debonding occurred. This debonding led to a very different model of the forces applied to the SRM casing. As a result, it was necessary to develop separate models for fragmentation when there was a large difference in the PBAN grain inertia and the casing inertia. Debonding due to inertia differences had to be considered when PBAN grain thicknesses were greater than 15 cm. These models are called "thick grain" and "thin grain." They will be discussed in turn.

1. Early MET Failure (Thick Grain Models)

The basic approach taken to the early MET failure effort was to propose a process for the SRM break-up, analytically model that process, exercise the model to predict resulting fragment velocity and azimuth and compare those predicted results to velocity and azimuth results inferred from the recovery location of the Titan 34D-9 SRM fragment. Specifically, the developmental models duplicated the geometry and mass of pieces 497, 538, 1109C and 1109G of Segment 1, SRM-1 of the Titan 34D-9.

The processess by which: the rationale for the analytical models were developed; these models were calibrated; and they were used to predict the SRM fragment velocities and azimuths resulting from various SRM abort events, are presented in the following subsections. These subsections are:

a. MODEL DEVELOPMENT
b. MODEL CALIBRATION
c. MODEL APPLICATION

a. MODEL DEVELOPMENT. While performing the calculations which led to the results shown in Figure 2, it was noted that the strain energy stored in the SRM casing was released very quickly after the initial fracture. The unit-strain energy stored in the PBAN is much less than that stored in the SRM casing. Because of its lower stored energy, lower sound speed, and greater mass, a considerable debonding force occurs at the PBAN-casing interface when the linear shaped charge (LSC) is initiated in a destruct action or a random-crack free-surface is generated. The resulting circumferential "twang" produces a high tangential and a lower but still significant radial casing velocity relative to the grain. This relative motion debonds the casing from the grain. Although the grain initially expands radially, it soon cracks and produces gas passages into the cavity which forms between the grain and the casing. After some initial grain oscillations, this cavity fills with hot gas from the chamber. The chamber gas exerts a force directly on the casing at this time.

1. Material Properties Effects. Variations in the material properties used in the Lagrangian model of the casing and fuel were modeled to investigate the debonding and cavity formation phenomena in greater detail. This model incorporated 182 casing zones and 546 PBAN grain zones. Material properties and property ranges used to exercise this model are presented in Table 2.

Figure 5 shows the geometry of a 34D casing which has undergone a casing failure, but has not yet suffered grain or casing fragmentation. The geometric model shown was described above and uses the UTC[1] properties shown in Table 2. This model was exercised to define the sensitivity of grain fragmentation to the values of PBAN material properties used. Detailed traces of the deviatoric stresses and the strain rates at a point four inches inside the inner diameter and 12.5 degrees from the initial-casing-crack free-surface are presented in Figure 6 and Figure 7.

The Von-Mises strain model invokes plasticity when three times the second invariant of the stress tensor (J_2') equals the material yield strength squared. Plasticity onset may be inferred from the times at which the deviators plateau. Examination of Figure 6 leads to the

Table 2. Properties of Materials Used in the TITAN 34D SRM

Material[1]	Casing	Grain (Solid)	Grain (Reaction Gas)
Type	D6A Steel	PBAN	PBAN
Equation of State			
Polynominal			
Young's Modulus, kbar	—	.0377[f]-0.121[g]	
Bulk Modulus, kbar	1670.	10.5-33.5	—
Poissons' Ratio	0.3	0.4994	—
Reference Density (ρ_o), gm/cc	7.86	1.775[a]	—
Gamma			
γ[b]	—	—	1.142
Specific Internal Energy, eu[b][c]	—	—	0.0672
Reference Density (ρ_o), gm/cc[b]	—	—	0.00571
Yield Model	Von Mises	Von Mises	—
Shear Modulus , kbar	816	0.0126-0.0403	—
Yield Strength, kbar	12.9	0.0087[f]-0.0483[g]	—
Spall Strength, kbar	1000.	100.	—
Elongation to Failure, %	10.	26.-52.	
Cylinder			
Areal Density, kg/cm	7.69[e]	—	—
Thickness, at 0 sec met, cm	typ. 0.95 min 0.88	87.2 fwd-100. aft	—
Height, at 10 sec met, cm	310.6	301.6	—
Inner Diameter, at 10 sec met, cm	304.8	122.7-148.1[b]	—
Outer Diameter, at 10 sec met, cm	306.6	304.8	—
Flange			
Areal Density, kg/cm	8.67[e]	—	—
Height, cm	33	—	—
Piece 497[d]			
Average Areal Density, kg/cm	1.258	—	—
Ave. Circumferential Extent, deg	57	—	—

[a]The rubber inhibitor is treated as having the same physical response as solid grain. The PBAN grain ρ_o is adjusted from 1.76 gm/cc to account for the presence of the inhibitor.

[b]Varies with burn time. See Figure 8 and Table 4 for typical geometry and pressure response.

[c]One eu is 10^{12} ergs.

[d]One of 12 pieces used to calibrate the model.

[e]Includes mass of ½ original rubber insulation.

[f]At 75°F. Thiokol Data[13].

[g]Results of dogbone tests at elevated strain rates. UTC Data[1].

34D-9 Initial Geometry
(Initial Chamber Pressure = 54.5 BARS)

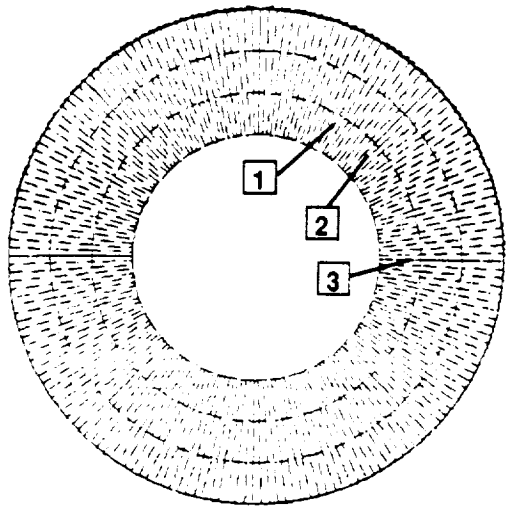

34D-9 Geometry 15 msec After
Initial Casing-Crack Free-Surface Formation

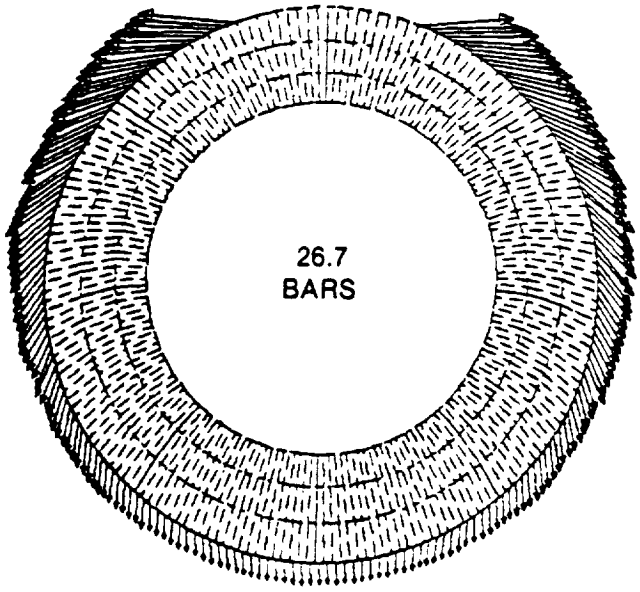

Figure 5. Model Used to Assess Sensitivity of Grain Fragmentation to PBAN Material Properties

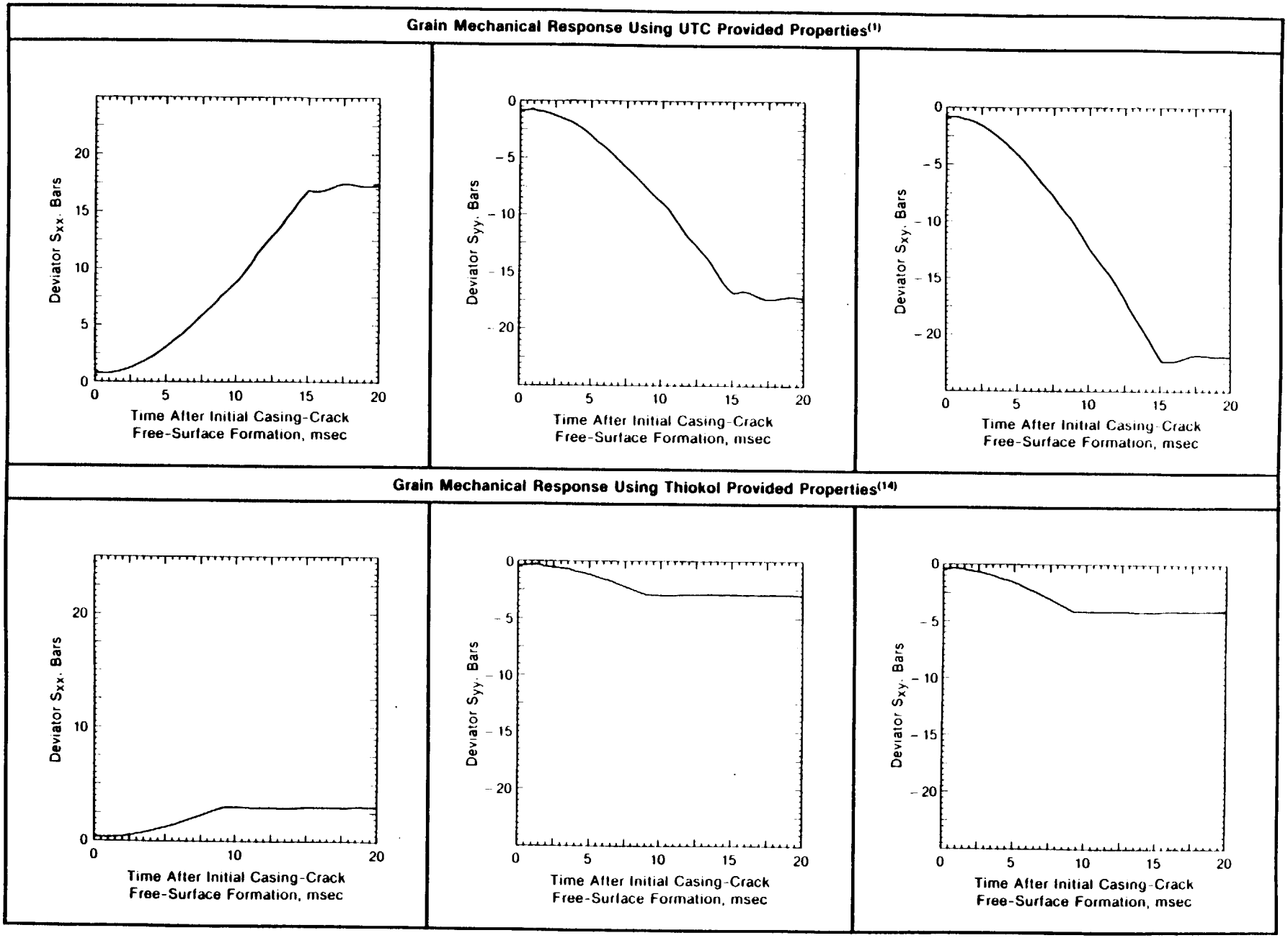

Figure 6. Comparison or Deviatoric Stress Time-Histories Using Grain Mechanical Properties Supplied by Thiokol and UTC.

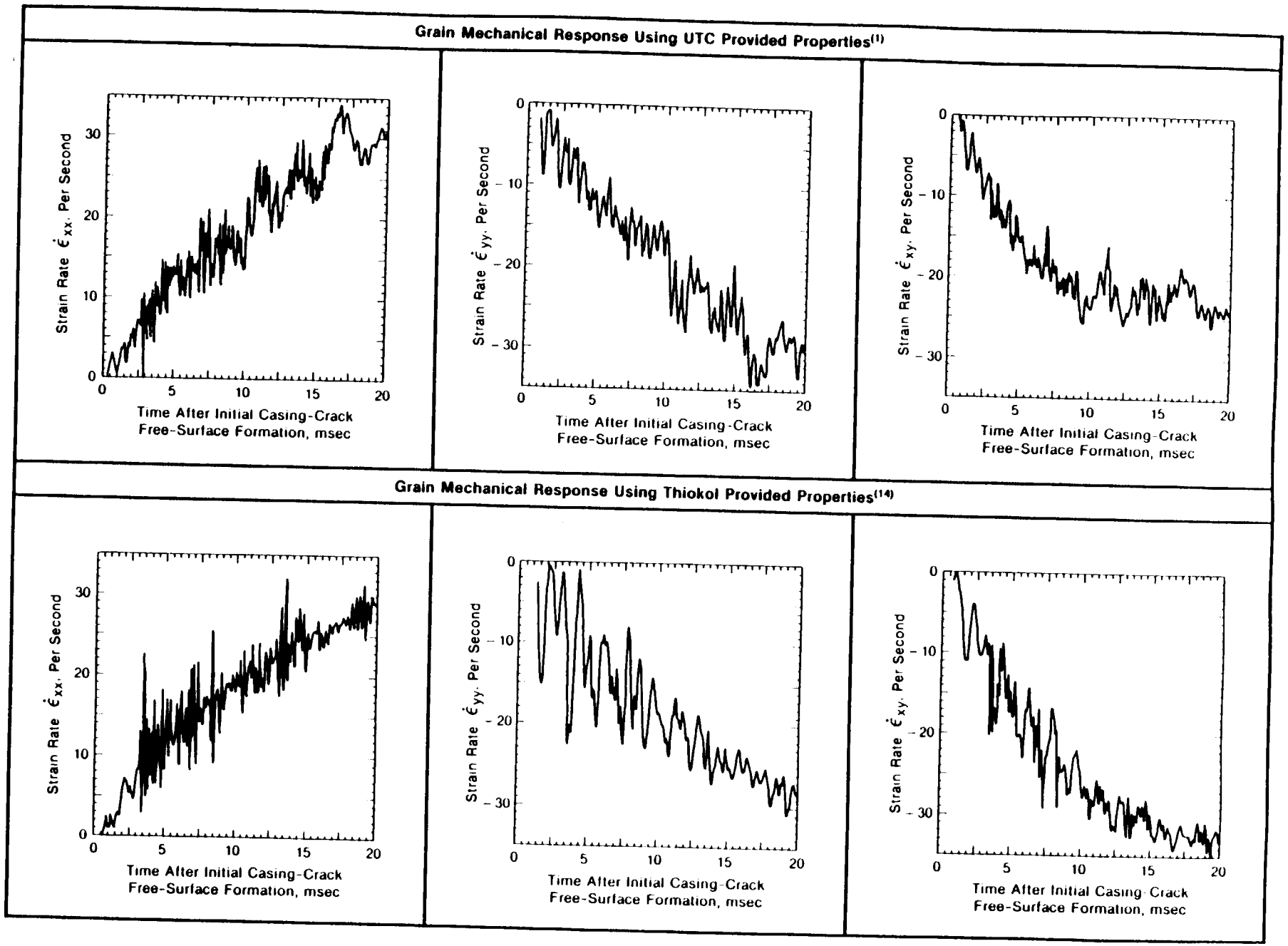

Figure 7. Comparison of Strain-Rate Time-Histories Using Grain Mechanical Properties Supplied by Thiokol and UTC.

conclusion that material properties uncertainty produces an uncertainty of a factor of two in the time of plastic flow onset.

Examination of Figure 7 shows that strain rates at the point of interest vary from essentially static to 30 per second. Elevated strain rates usually affect only the traditionally non-liner properties of a material; however, with PBAN the effects of the large implied elastic-strain regime are uncertain. The material properties of the PBAN are important in establishing a proper physical model. This material is rubber-like and has a reported Poisson ratio of 0.4992. Poisson ratio is normally a small strain concept. It is usually determined by placing thin "poker chip" type samples in tension and measuring their resulting height decrease. Table 2 shows that the yield strength of PBAN is between 20 and 30 percent of the reported Young's modulus. This would imply the presence of a very large elastic strain prior to the onset of plasticity. It is unlikely that Young's modulus would remain linear over such a range of elastic distortion; however, no strain-dependent modulus information was available. Although it is not shown in Table 2 the further implication is that about half the strain-to-failure would occur in the elastic portion of the loading curve; however, one would have to know the nature of the unloading curve to say this with certainty. The Thiokol data show that the PBAN strain to failure is anisotropic. No attempt to incorporate anisotropy into the model was made.

The effects of large elastic strains prior to plasticity onset are illustrated in Figure 8. Effective stress is defined as $\sqrt{3}\, J_2'$. Note that a large amount of PBAN has exceeded the plastic flow criteria relatively early in the event. An attempt to develop a failure criteria was made and is presented in Figure 9. It is assumed that the failure strain given in Table 2 sources are engineering strains, $(l-l_0)/l_0$, rather than the natural strain, $\ln (l/l_0)$, used in PISCES. Figure 9 shows a composite curve of the elastic and plastic strains obtained from assuming linear elastic behavior for PBAN prior to the onset of the PISCES predicted plasticity. Note that fragmentation is strongly dependent on the value of strain selected as a failure criteria. A further limitation of any linear elastic model with a Poisson ratio nearly equal to 0.5 in that there is no PdV work involved. Given the available properties of PBAN, this implication seems unlikely. It was concluded from these results that a reliable grain fragmentation model

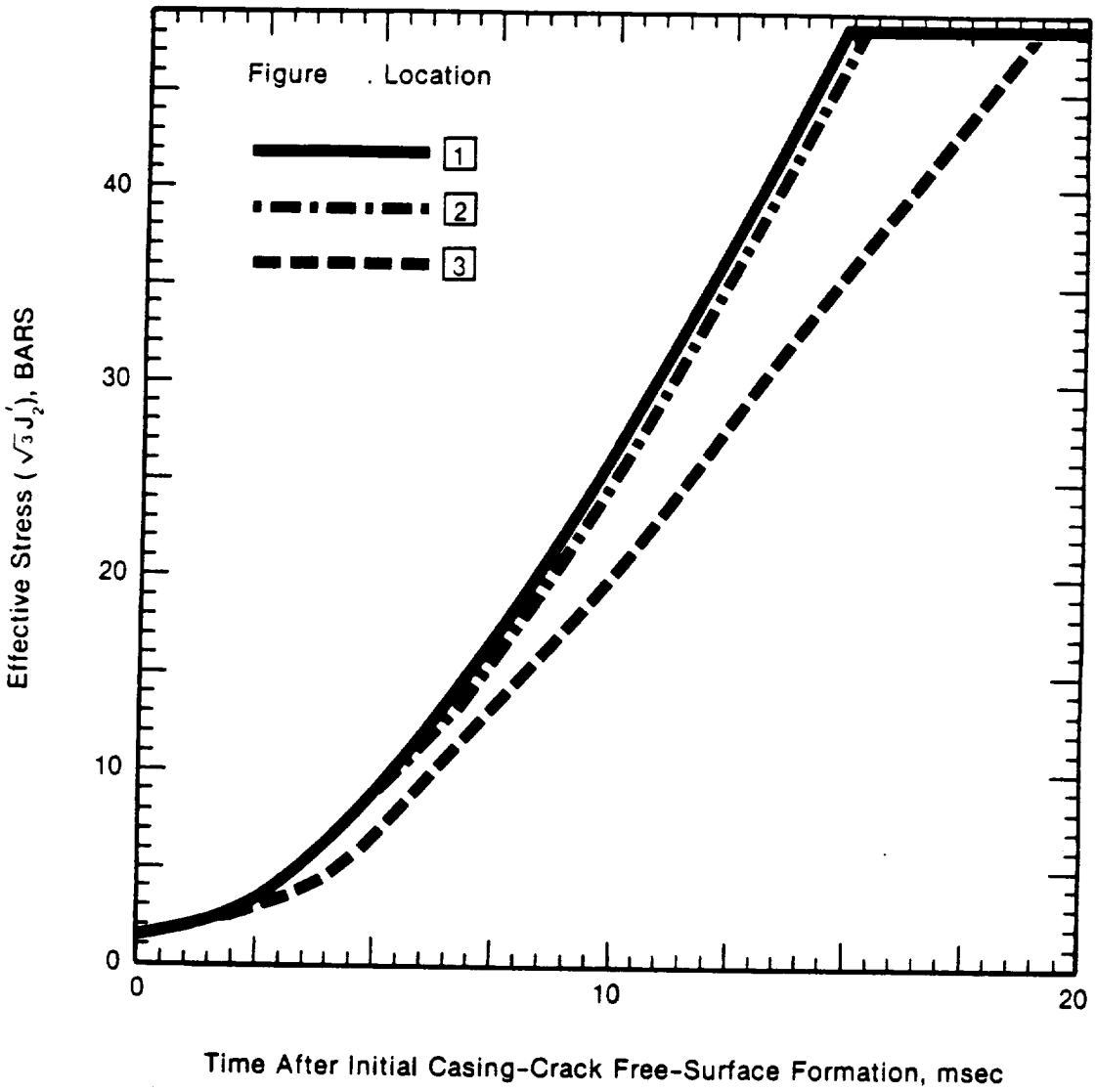

Figure 8. Time-History of Effective Stress at Three Locations Shown on Figure 5

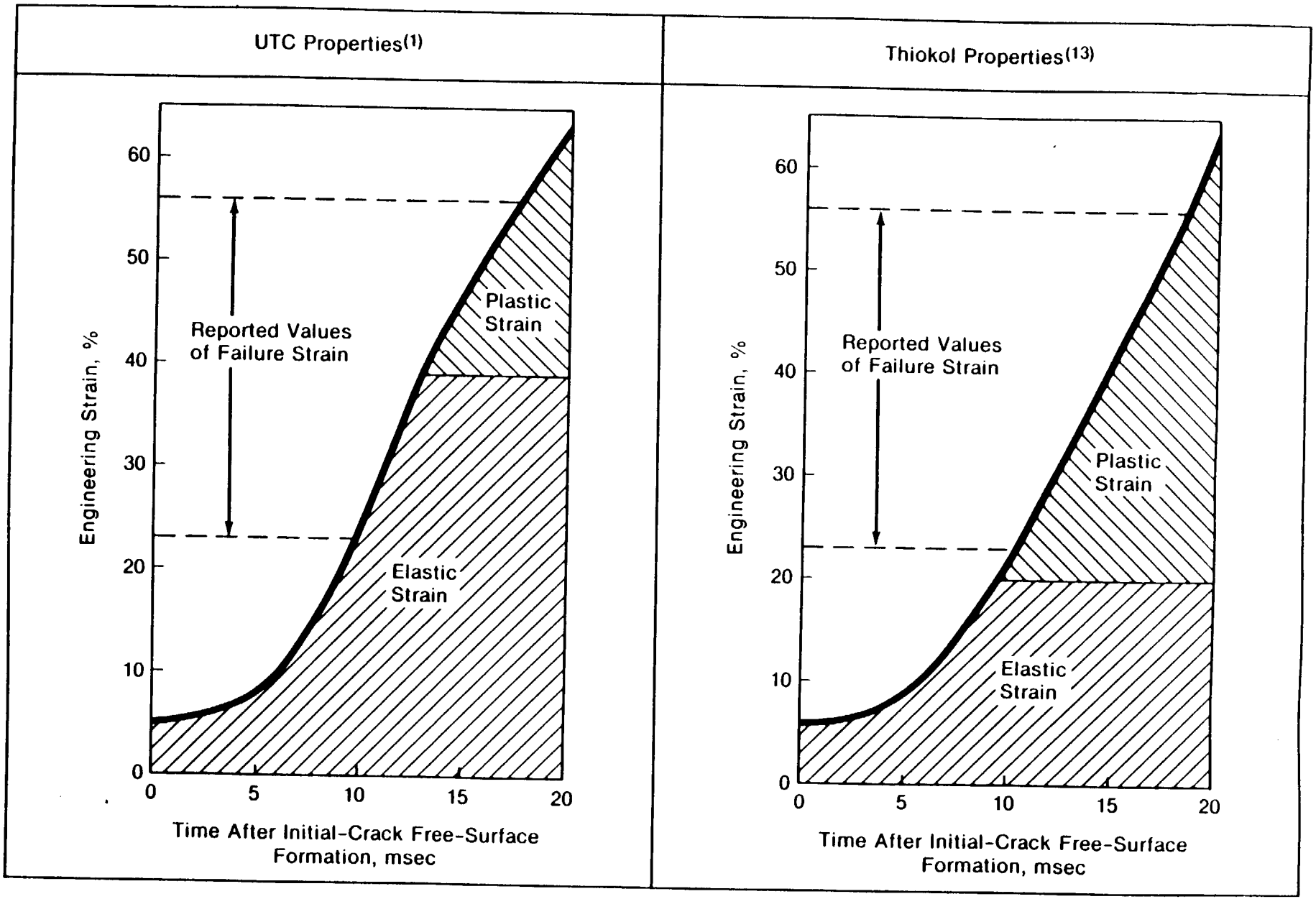

Figure 9. Time-History of Strain at Location [1] Figure 5

could not be generated because there were too many uncertainties in the fracture mechanics of PBAN.

Additional analyses were performed to see if the model could be desensitized to the effects of grain fragmentation. Slide line logic had already been incorporated in the model discussed above between the casing and the grain. The purpose of this logic was to investigate the potential effects of tractive forces (friction) at this interface. Additional slide line logic was provided between four 45 degree sections of grain to provide time-zero grain defects. It was reasoned that a material with a Poisson ratio of 0.4994 would undergo considerable circumferential growth while undergoing radial contraction. As shown above, failure does not occur from hydrostatic loads; it occurs from deviatoric stresses. The actual value of deviatoric stress at which the grain would fail would be difficult to predict. As was shown, there are few, if any, reliable data for the value of PBAN yield strength at destructive-disassembly strains and strain rates. The slide lines at the 0, 45, 90, 270 and 315 degree location would give witness to the time at which the compressive circumferential force was lost. This witness would manifest itself as a gap opening between the grains. It was also reasoned that gas would begin to flow from the chamber into the cavity which forms between the grain and the casings at the time at which these gaps begin to open.

The development of the SRM-casing "twang" is shown in Figure 10. Details of selected interesting areas of Figure 10 are shown in Figure 11. The particle velocity vectors show that activity has traversed 90 degrees of casing in the first 500 μsec after the generation of the casing-crack free-surface. A substantial cavity is seen developing 180 degrees from the crack initiation site after 2.0 msec. This cavity persists at 4.5 msec since the grain dilation, because of its higher inertia and lower wave propagation speed, has not yet accelerated sufficiently to keep up with the casing. The expansion of the casing inner diameter can be noted after about 2.5 msec.

An algorithm was needed to relate chamber pressure to chamber inner diameter. The argument could be made that increasing inner diameter causes increased burning surface which would raise the mass flow rate of gas into the chamber. Conversely, increasing chamber inner

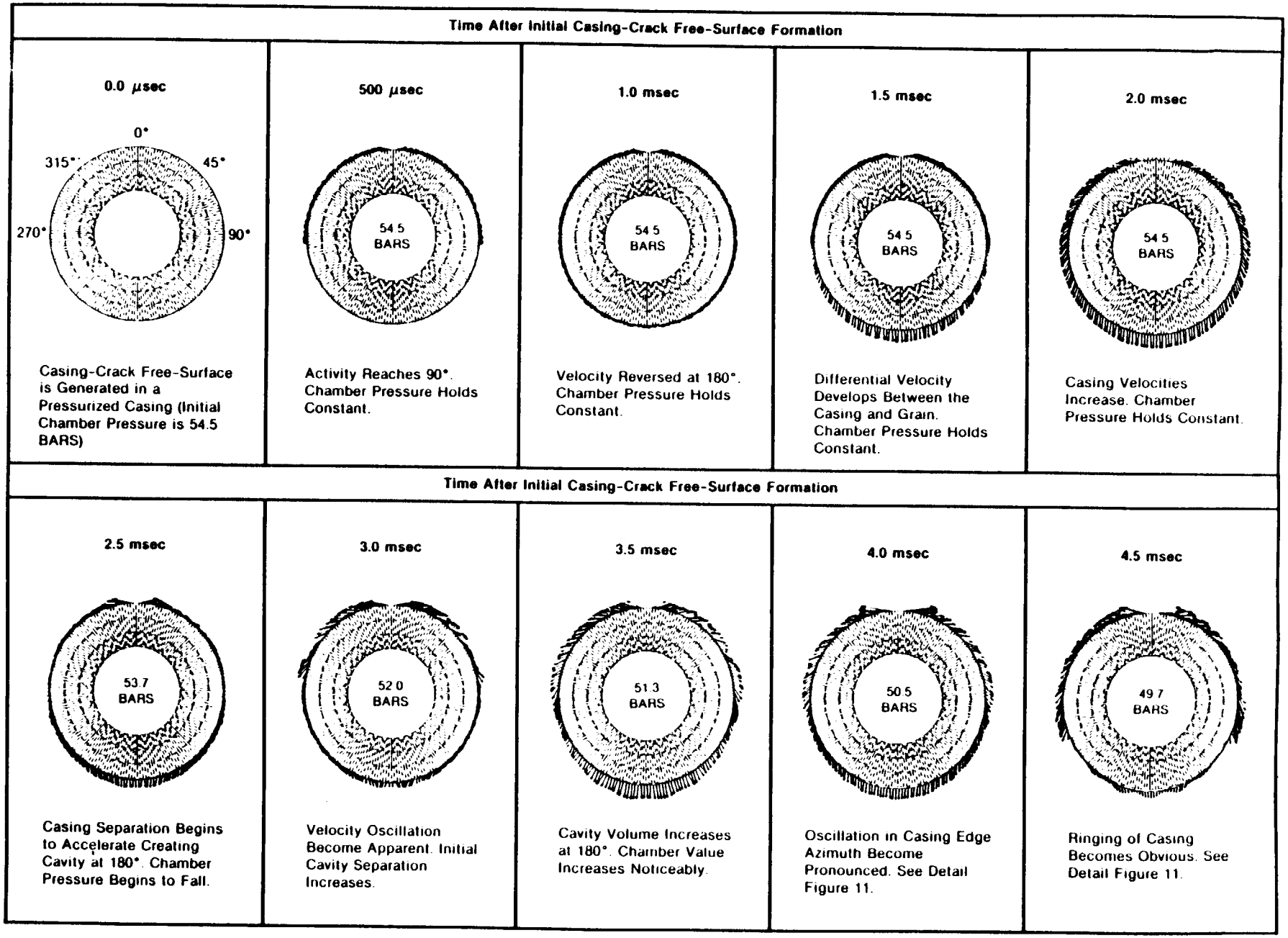

Figure 10. TITAN 34D SRM Casing Geometry and Particle Velocity Time History

Detail from Figure 10 Showing Retrograde Motion of
Casing-Edge Vectors at Casing-Crack Initial Free-Surfaces

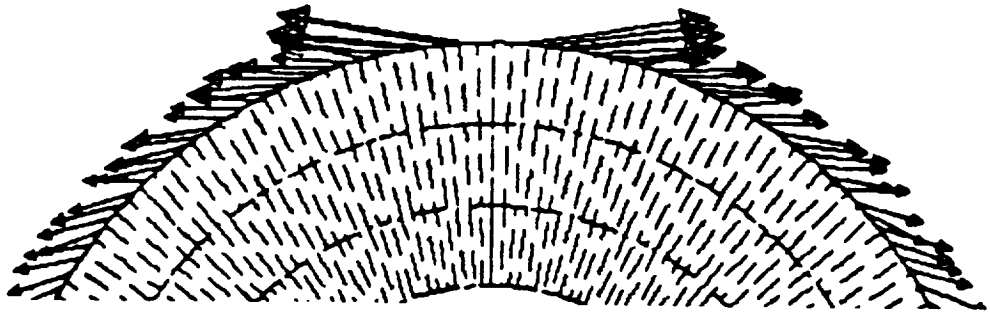

Time = 4.0 msec

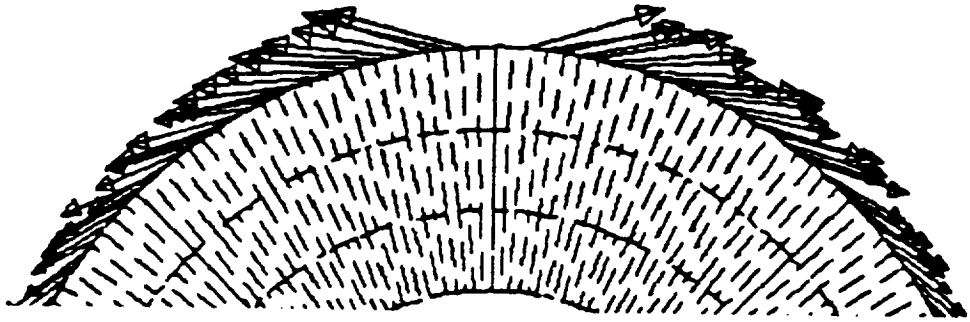

Time = 4.5 msec

Detail from Figure 10 Showing Persistance
of Cavity Between SRM casing and Grain

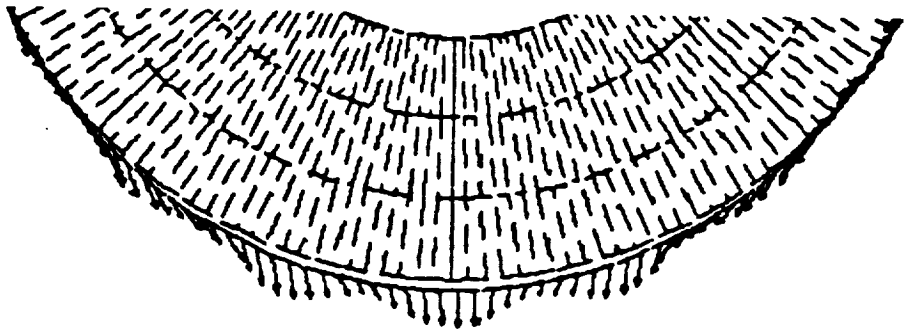

Time = 4.5 msec

Figure 11. Detail of Indicated Zones of Interest in Figure 10

diameter would increase the chamber volume and this would reduce the burning rate by the cube root of the chamber volume ratio. Since both these effects would take time, and the total event time could be recorded in tens of milliseconds, the authors evaluated the earlier work on short-time energy addition effects and chose to assume that the mass of the gas in the chamber, its gamma and it specific internal energy remained constant until radial outflow from the chamber began. The time at which this radial flow began would be taken as the time that gaps opened between the PBAN slide lines at the 45 degree incremental locations. Armed with this logic, the authors intrepidly assumed that the chamber pressure simply tracked the chamber volume as the grain inner diameter increased.

The results shown in Figure 12 were obtained using the model described above. Note that 10 msec after casing-crack initiation, there are no gaps in the grain. After 15 msec, however, these gaps have clearly formed. It was felt that friction at the casing-grain interface may have an effect on the time at which gaps developed. The effect on gap-opening delay-time of using coefficients of friction of 0.5 and 1.0 at the casing-grain interface are also shown in Figure 12. Note that interfacial friction causes significant distortion of the grain.

It was reasoned that the grain distortion caused by the casing-grain interfacial tractive forces would produce large stress discontinuities at the outer diameter of the grain. These forces would then produce a series of flow channels near the casing edge as the stress discontinuity alternately built up and was relieved by crack initiation. As has been shown, the physical properties of the PBAN grain are not well known and the grain fragmentation times are very sensitive to these properties. As a result, the fracture mechanics of the grain cannot be well described, and a pathway to a reliable grain fragmentation model was not obvious. The authors wished to develop a model which was as insensitive to the uncertainties of the PBAN fracture mechanics as possible. While we were aware of the physical realities of grain flow passage development delay, we felt that the model described above was too uncertain a basis for predicting fragmentation time and we opted for a modeling method which would lump the uncertainty in grain fragmentation time with the uncertainty in a number of other variables to produce a simplified statistical data base. It is with this line of reasoning that the

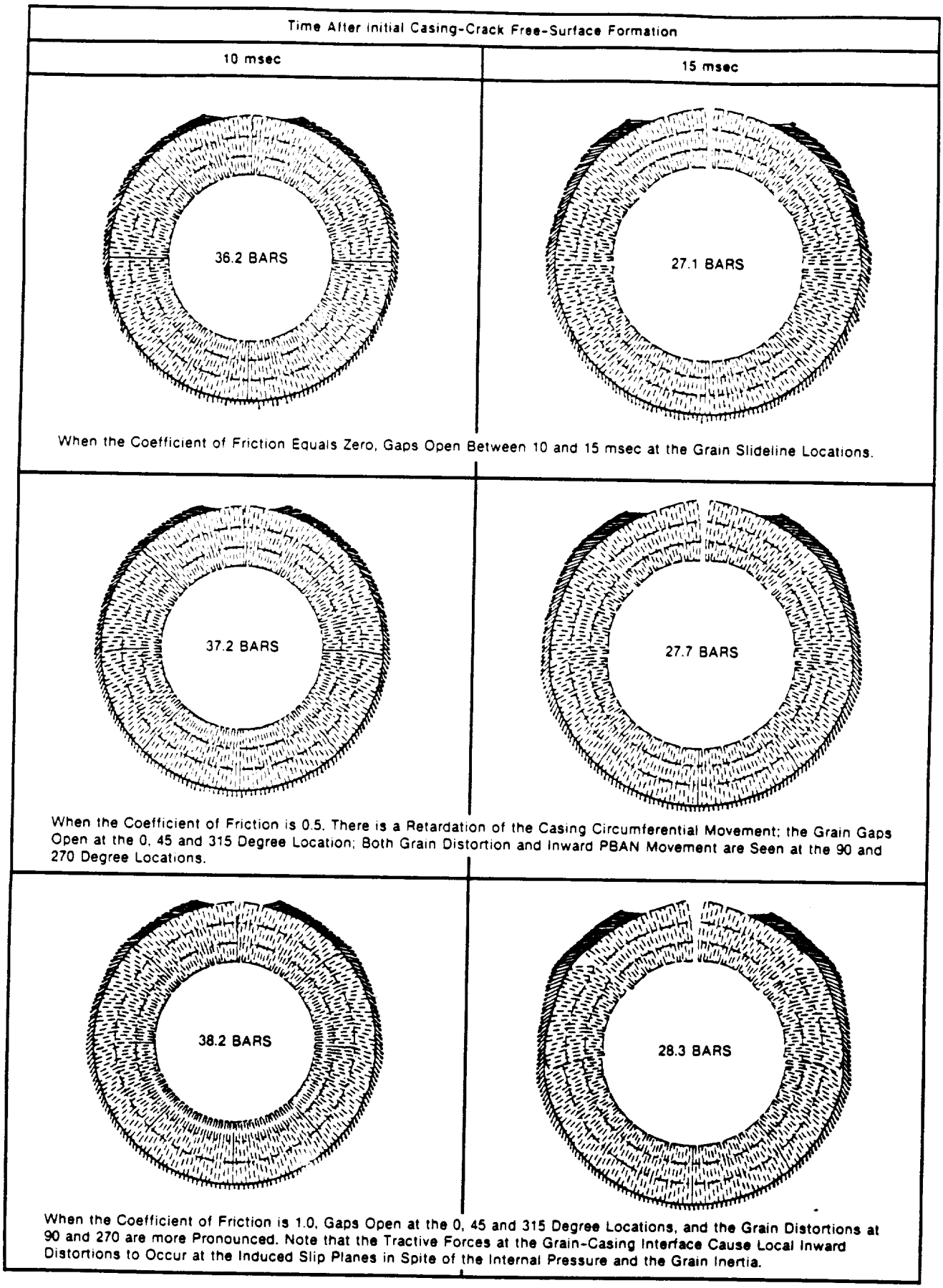

Figure 12. Effect of Casing-Grain Interfacial Tractive Forces on Grain Fragmentation, Casing-Grain Relative Motion and Chamber Pressure

model used to produce the input to the Shuttle Data Book was developed. The details of this model will be presented in a subsequent section.

2. Models Proposed by Other Investigators. Some calculational methods currently in use are based on the assumption that the total available chamber impulse may be applied directly to the SRM casing to obtain fragment velocity. This assumption is incorrect because it invokes a static pressure field and ignores the pressure drop and mass losses which occur between the chamber and the casing-grain cavity. In the highly dynamic flow field which occurs during SRM fragmentation, it is patently unreasonable to assume that the velocity of the gas flow into the region between the grain and the casing is subsonic. The pressure ratio which exists between the chamber and this cavity will be determined by the physical properties of the gas and the flow area into and out of the cavity. Given that these flows will be supersonic, the pressure ratio between the chamber and the cavity will be about 0.5. This means that the pressure acting on the casing fragment will be about one-half of the chamber pressure. Because of the importance of the gas flow into the cavity, a very detailed (one cm square zoning) model of the cavity and chamber flow interaction was developed to test this postulate and to assess the magnitude of the effective static pressure which could occur in this cavity during SRM fragmentation. The authors chose to model this cavity development at the location of the initial fracture; however, this is not a requirement of the scenario. The model is typical of any grain-crack casing-edge interaction.

In addition to the above, several investigators have pointed out that there is a gap between the grains where each cylinder is joined. Gas from the chamber can flow through that gap and into the cavity formed between the fuel and the casing. Indeed, there can be a three dimensional flow field; however, this flow field must be properly defined. A detail of this gap is shown in Figure 13. Examination of this figure shows that the flow area to feed the grain-casing cavity is quite small at early MET. Burning increases the width of this gap and decreases the length of the gas flow path as MET increases. Thus, at early MET the ability of the available mass flow rate to maintain cavity pressurization by this method will be highly questionable. At late MET this cavity pressurization method becomes more reasonable. It should be noted that the cavity produced at the 180 degree location shown in Figure 11 can

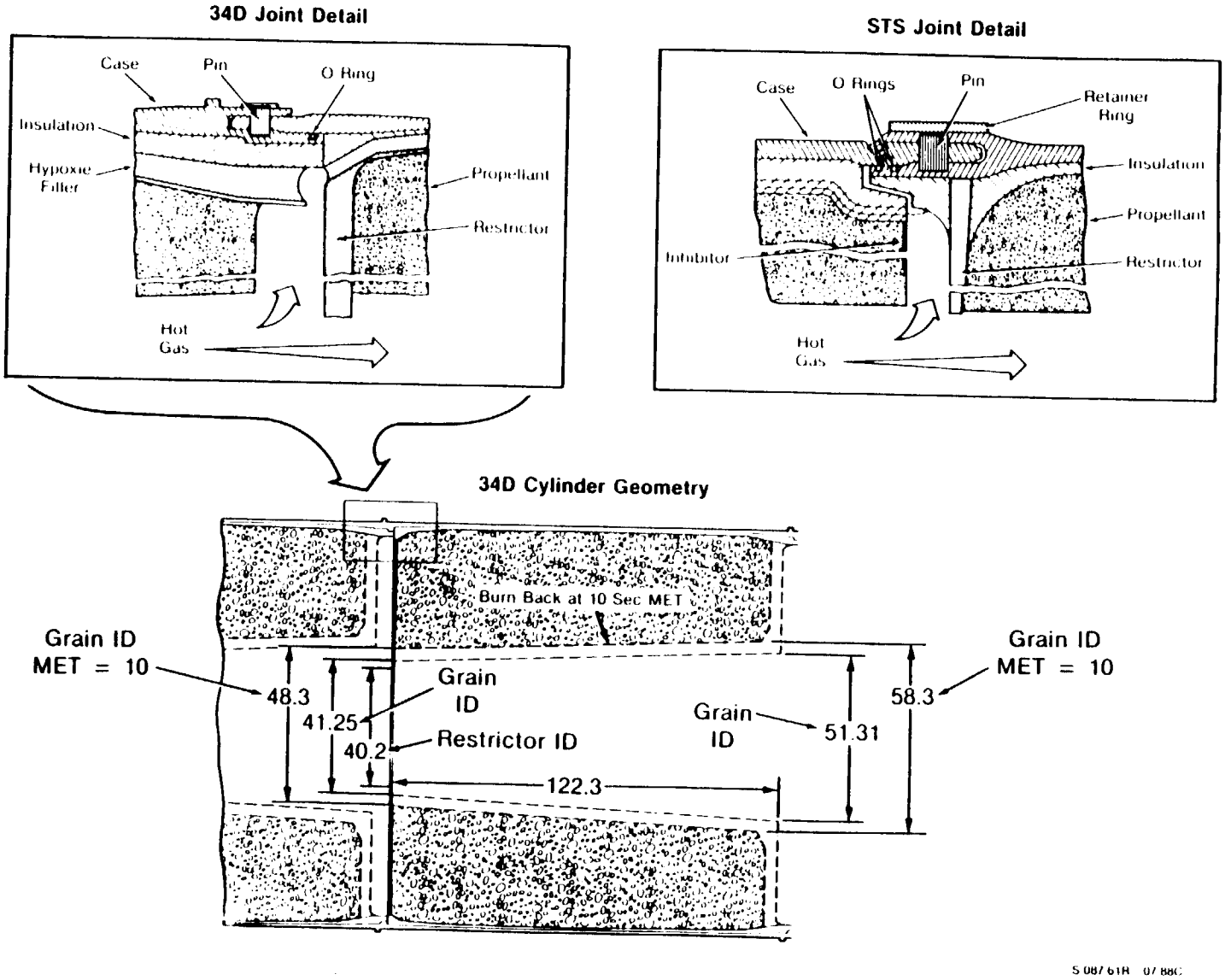

Figure 13. Typical SRM Cylinder Geometry Showing 34D and STS Joint Details

communicate with the gas in the gap between grains. This could pressurize the cavity until the grain flow closed the cavity or it could prevent the grain from expanding by equalizing the pressure. If the pressures on the grain inner and outer diameters equalize, the grain outer diameter will transiently contract because of the greater PA force. This would tend to increase the cavity volume. In any event, it is unlikely that this flow pathway could keep the cavity pressurized after initial casing displacement.

Examination of Figure 13 also shows that the flange is a significant reinforcement. The areal density of the flange region is twice that of the casing. Further study of Figure 13 shows that the Titan 34D-SRM casing flange is somewhat more robust than the STS-SRM flange. In addition, the 34D-SRM has no LSC on the flange. The STS-SRM is fitted with a 1000 grain/ft HMX-LSC along the entire length of the casing (except for the three aft cylinders) including the flange. The likely development of the casing grain cavity formation and SRM fragmentation is shown in three dimensions in Figure 14.

Given the greater areal density of the flange region and, in the case of the 34D-SRM, the lack of an LSC, it is difficult to see how gas flowing supersonically from the chamber could negotiate the right angle turn into the cavity from the zone between the grains. Clearly the higher areal density of the flange region will result in a lag in its radial expansion relative to the casing center region. Further, it is unlikely that, once fractured, the PBAN grain will remain stationary during the disassembly process. The grain is acted upon by the chamber pressure on its inner diameter and by the cavity pressure on its outer diameter. It will remain stationary only if the forces generated by the pressures acting on these areas are equal. The maximum cavity pressure will be set by a complex material balance between what flows into and what flows out of the cavity. The supersonic nature of the flow field must be modeled analytically and any assumption of equal cavity and chamber pressures is demonstrably incorrect. Preliminary calculations showed that additional gas flow passages through the grain would begin to develop in the first 5 msec after initial grain failure. Although the authors chose to provide initial cracks in the fuel model, these cracks were not assumed to be caused by the LSC. They were assumed to result from the expansion of the grain caused by the chamber pressure acting on the grain inner diameter, by the radial tensile waves generated by

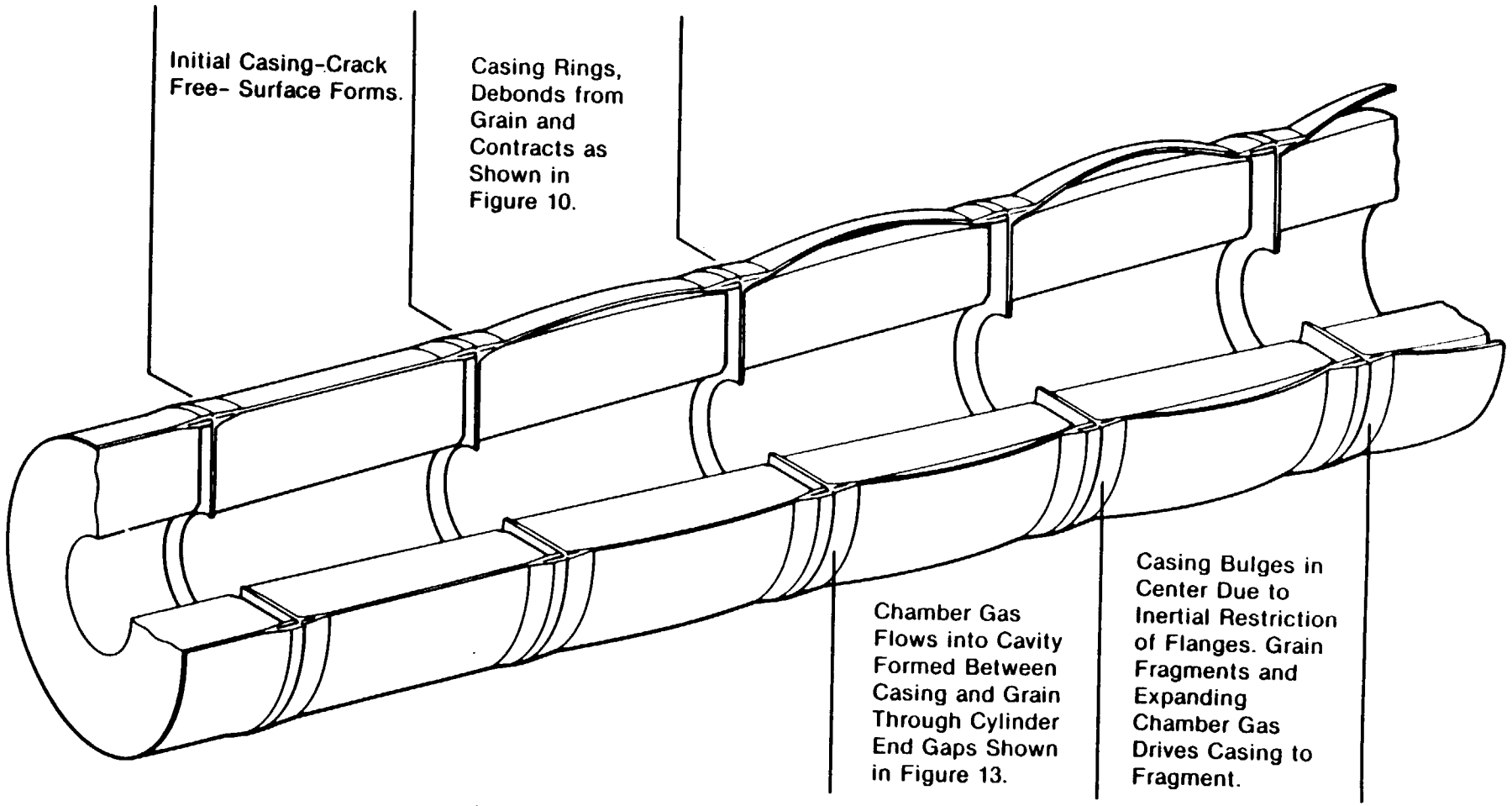

Figure 14. Probable Three Dimensional Scenario for SRM Fragmentation

the release of the casing hoop constraint, and by the stress discontinuities generated by the tractive forces at the casing-grain interface. It was felt that any delay in grain fragmentation may delay the initiation of chamber pressure decrease but such a delay will change its initial magnitude only to the extent that the chamber volume increases. Therefore, the zero time used in our models is the time of first crack propagation from the casing to the chamber, not the LSC initiation. The authors felt that the uncertainties associated with the actual fracture mechanics justified the use of a two-dimensional radial flow model which ignored longitudinal flow into the cavity. It is the authors' judgement that this assumption does not significantly affect the results predicted for the range of various SRM fragment environments studied.

3. Model Used for Shuttle Data Book Input Geometries. A simplified 2-D model of the actual problem geometry is presented in Figure 15. This model does not attempt to determine grain fragmentation time, nor is it dependent upon a precise prediction of the actual chamber pressure at the time of grain fragmentation. The assumption is that the maximum chamber pressure is available to accelerate the casing fragments at the time of casing failure. This assumption should result in the prediction of the highest possible fragment velocity. While this model does not include cavity feed from the cylinder ends (z-flow), it does include stagnation and circumferential flow effects. In this model, the degree to which a casing fragment is in the lee of a grain fragment affects the ability of the pressure which acts on the fragment to reach its theoretical maximum. Fragment-to-grain orientation then becomes a statistical variable by which to account for the observed fragment velocity distribution. The assumption of a casing lip projecting into the supersonic flow stream provides a mechanism for pressurizing the cavity. As previously noted, it is not a requirement that this lip be placed at the location of the LSC or the initial casing-crack free-surface. It is only necessary that it occur opposite a flow passage which has been created by grain fragmentation. This mechanism produces a pressure acting on the fragment area which is believed to be essentially correct regardless of the details of the flow and fragmentation process. A detail of the one cm square zoning coupled Eulerian-Lagrangian model which shows the interaction of the various flow and mass components is presented in Figure 16.

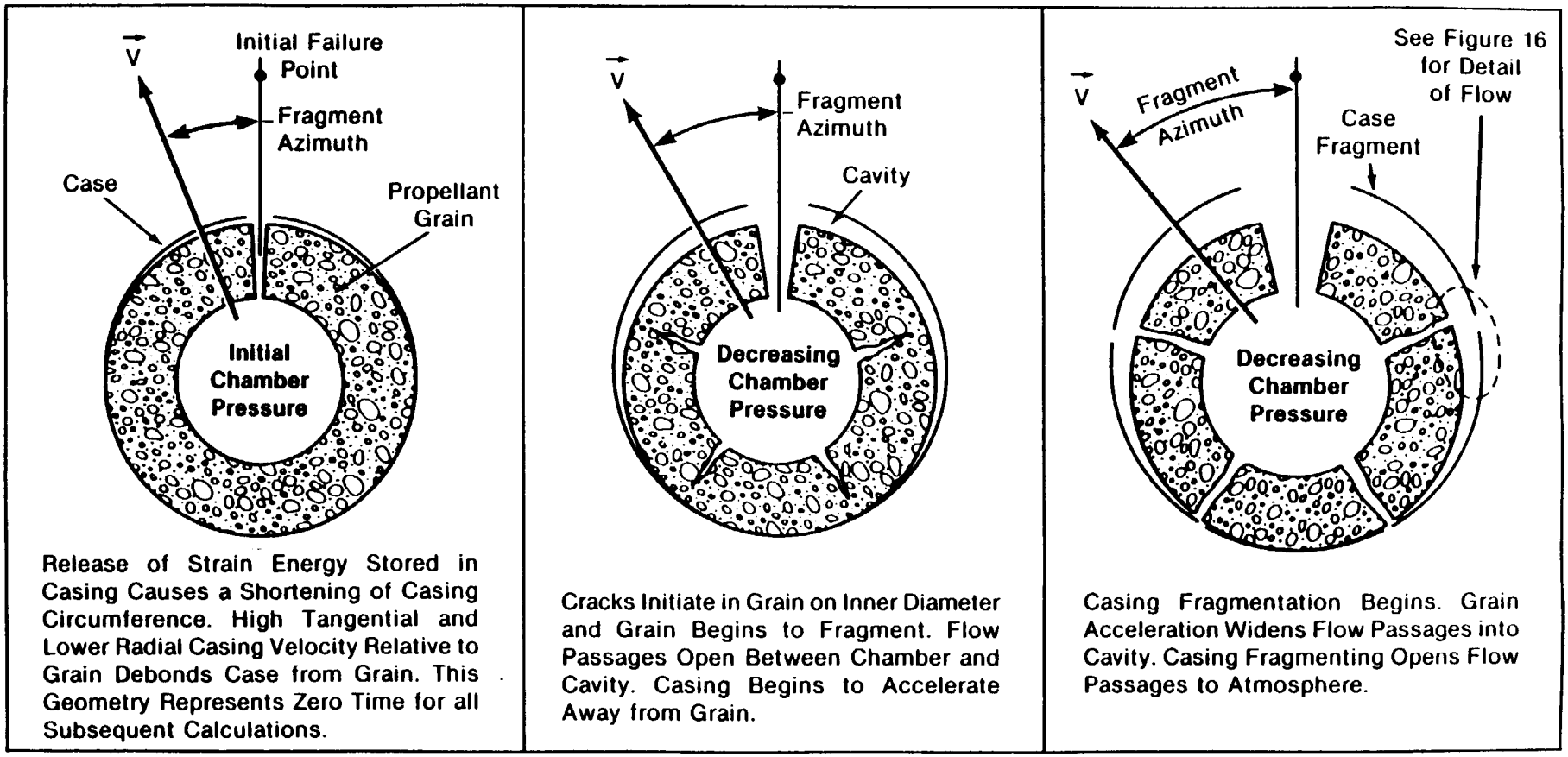

Figure 15. Early-MET Model Formulation Showing Case Separation, Cavity Development, Grain Fragmentation and Casing Fragmentation

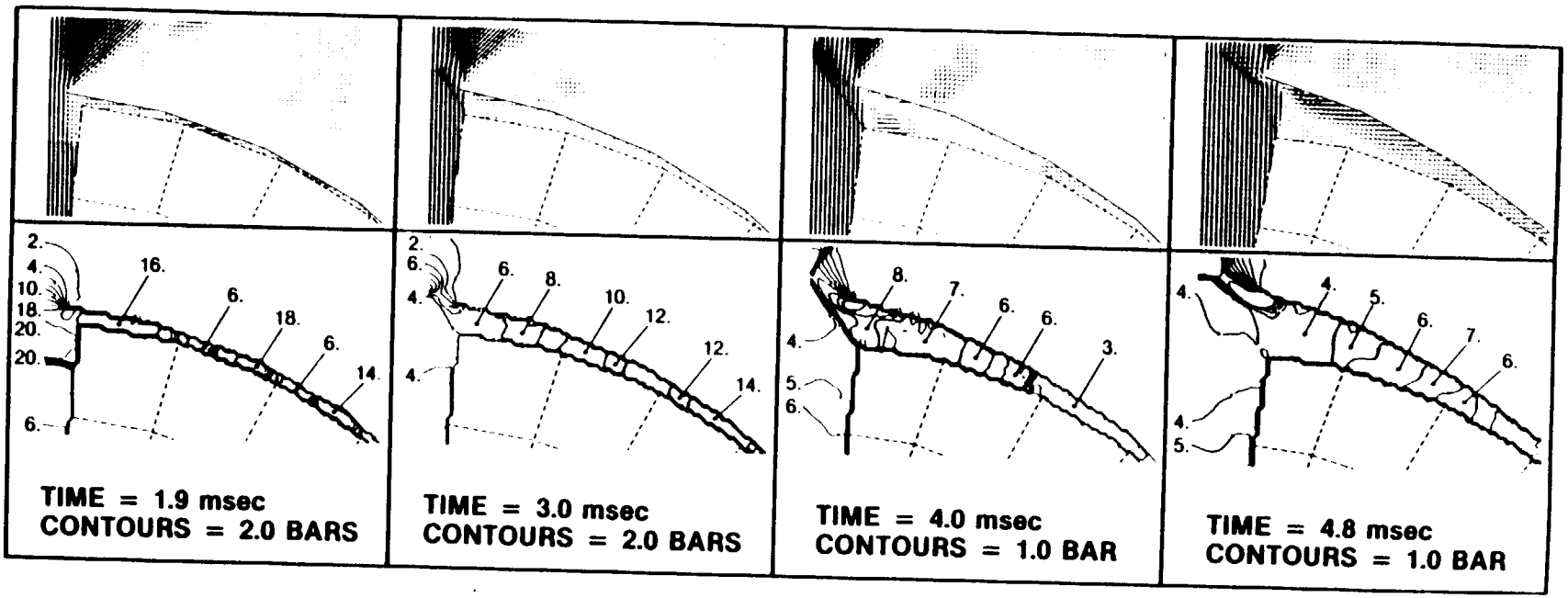

Figure 16. Developing Flow Field in the Grain-Casing Cavity at Various Times After a 34-D SRB Casing Failure at 10 Seconds MET

Calculations of this type were performed for a number of SRM geometries at various mission elapsed times (MET). These calculations varied SRM diameter, casing areal density, grain thickness and chamber pressure. They were generated to provide forcing functions for a study of the sensitivity of the fragmentation process to these variables. While assembling these results, Peter Jaffe[2] noted that it was possible to normalize across the MET and SRM-type domains and to produce a set of curves which related cavity pressure to chamber pressure for any MET and time-after-initial casing failure. These curves are presented in Figure 17. The existence of a single functional relation for cavity and chamber pressures across the MET and SRM-type domains greatly simplified the problem of predicting SRM fragmentation response. Because of this relation, the computational process could eliminate the Eulerian portion of the problem. The casing fragmentation process could be approximated by applying the appropriate pressure from Figure 17 as a stress boundary to the grain inner diameter and outer diameters, and to the casing inner diameter. The extant atmospheric pressure was applied to the casing outer diameter to develop the appropriate net casing accelerating force.

b. MODEL CALIBRATION. It was necessary to calibrate the early MET model to establish its credibility. No early MET STS-SRM failures had occurred; however, the Titan 34D-9 had failed at 10 seconds MET. It was felt that the 34D-SRM would be similar to the STS-SRM in fragmentation response. The Titan 34D-9 event was useful not only in that it provided fragmentation information against which the analytical model could be calibrated, but also because it contained both a randomly failed booster (SRM-2) and a range destructed booster. As in the case of the 51[12], the 34D-9 casing had fragmented into large sections which could be defined approximately as octants, quadrants and halves of the casing. Only the single randomly failed segment of SRM-2 was fragmented into a significant number of pieces smaller than an octant. There were obvious detail differences between the 34D-SRM and the STS-SRM. Nevertheless, it was reasoned that if good predictions of the 34D-9 fragment environment could be made the efficacy of the modeling process would be established and it could be extended to predict STS-SRM fragmentation response.

A detailed model of the Titan 34D-9 event was prepared. The properties of the materials used in the preparation of this model were previously presented in Table 2. The

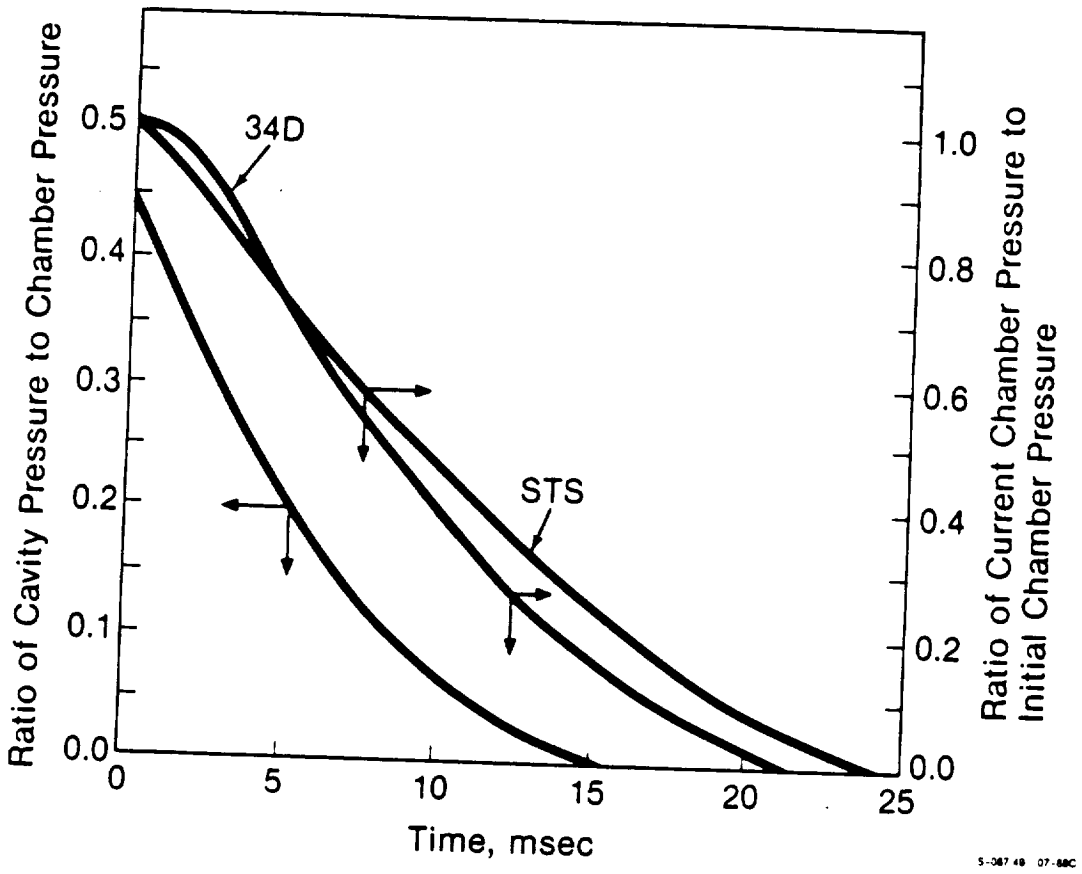

Figure 17. **Normalized Chamber and Cavity Pressure-Time-Histories — After Jaffe[2] (This figure is based on Eulerian-Lagrangian coupled calculations the details of which were shown in Figure 16.)**

model geometry approximated that of the fragments from SRM-1 and SRM-2 known to have been created in the abort. Each of the five SRM segments was zoned into fragments of the observed circumferential extant. The initial stress distribution within the casing and PBAN was developed by applying the chamber pressure extant at 10 sec MET as a stress boundary to the inner surface of the PBAN prior to the initiation of the casing failure. A casing fault was introduced into the model and the relevant cavity pressure time-history from Figure 17 was applied to the casing inner diameter and the grain outer diameter. The relevant chamber pressure time-history was simultaneously applied to the grain inner diameter. Again note that zero time in all the time-history curves is the time at which the first continuous crack develops between the chamber and the casing.

The development of the fragmentation pattern typical of the boosters studied is shown in Figure 18. This fragmentation pattern is for segment 1 of SRM-1. The sensitivity of fragment geometry and velocity to the time after initial fracture at which fragmentation occurs is shown in Figure 19.

The x and y velocity of each Lagrangian zone are calculated within the code and archived. An edit routine sums the squares of the x and y velocity of those models which constitute a recovered fragment. The velocity of a fragment then is determined by extracting the square root of the sum of the squares of the x and y velocity. The azimuth of a fragment is calculated by determining the arctan of the ratio of fragment x and y velocity and relating this angle to the proper quadrant. A study of Figure 20 is especially instructive. It shows, in general, that:

1) Fragments adjacent to the initial failure point attain the highest velocities.

2) Given the same orientation to the point of initial failure, smaller fragments reach higher velocities than do larger fragments.

3) Up to a point, fragment velocity increases with increasing time between initial casing failure and casing fragmentation (fragmentation times).

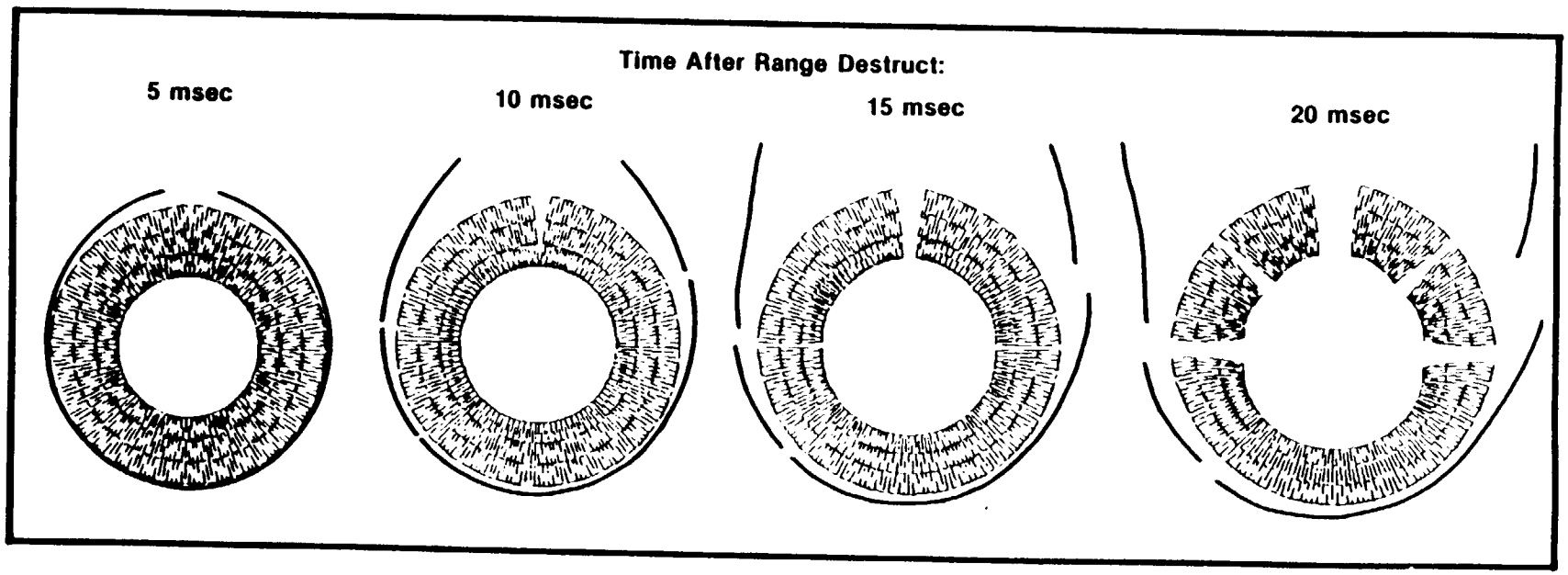

Figure 18. 34D-SRM Casing Geometry at Various Times After a Range Destruct Action and for an Assumed Fragmentation Time of 5 msec After Initial Casing Failure

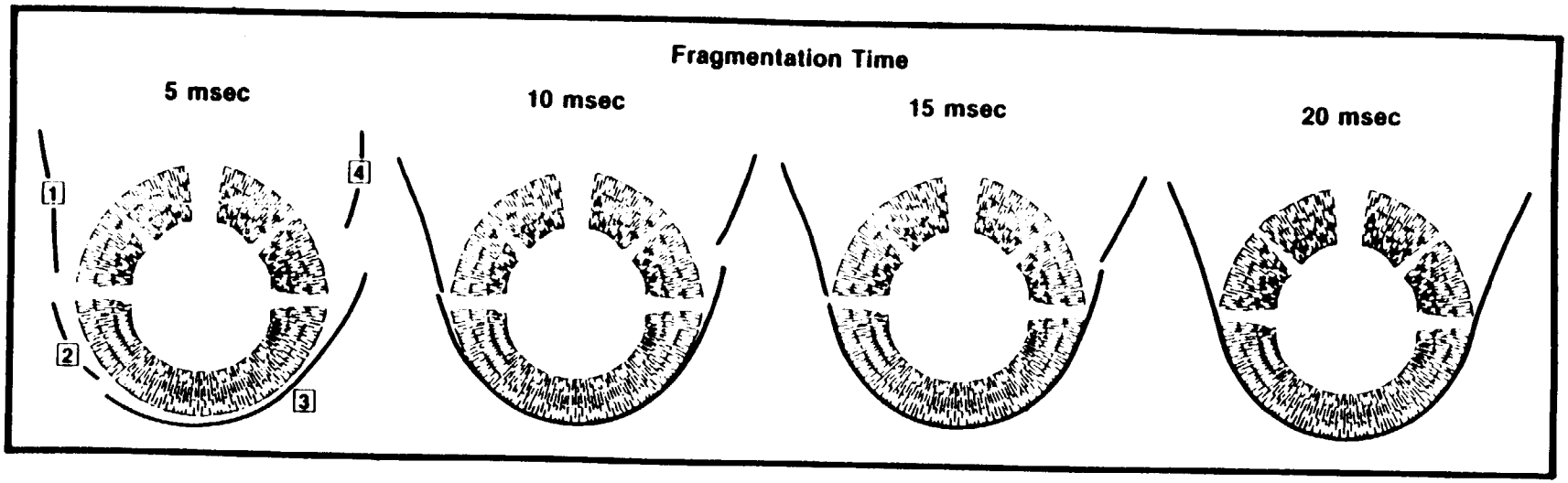

Figure 19. 34D-SRM Casing Geometry for Four Assumed Fragmentation Times 20 msec After a Range Destruct Action at 10 Seconds MET

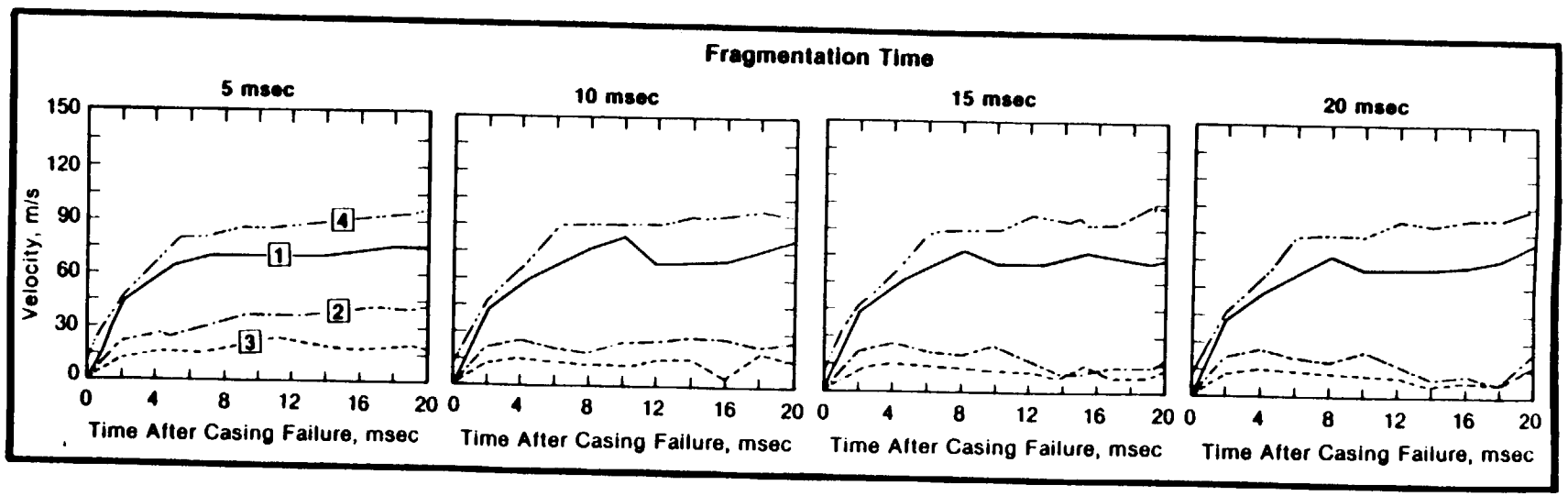

Figure 20. Time-History of Fragment Velocities Resulting from the Range Destruction of a 34D-SRM for Four Assumed Fragmentation Times at 10 Seconds MET (Squared numbers refer to fragments shown in Figure 19)

Further examination of Figure 20 shows that maximum fragment velocity is not a strong function of casing fragmentation time for early-MET range- destruct cases. It is difficult therefore to establish casing fragmentation time by comparing the predicted fragment velocities to the velocities inferred from the range and the abort positions at which the fragments were recovered. It was reasoned that fragment azimuth might be more sensitive to casing fragmentation time than velocity would be. The azimuths of the fragments presented in Figure 20 and Figure 15 are presented in Figure 21. Examination of Figure 21 shows that the azimuth of the fragments adjacent to the initial fracture surface are relatively sensitive to casing fragmentation time. In addition, it is seen that the azimuth of the smaller fragment (fragment 4) is more sensitive than is the azimuth of the larger fragment (fragment 1).

Given that the smaller fragment adjacent to the location of initial casing failure is the most sensitive indicator, it was reasoned that grouping the four fast fragments (fragment 4) shown in Figure 20 might be instructive. The results of this cross plot are shown in Figure 22. It is seen that fragment velocity is not a sensitive indicator of fragmentation time but azimuth is.

A detailed comparison of the results of sensitivity calculations to the observations made for the 34D-9 event is presented in Table 3. The effects of arbitrarily reducing the maximum predicted cavity pressure to capture the observed data base are also shown in this table.

The computational methods described slightly over-predicted the maximum velocities observed in the 34D-9 event. Detail differences, which were noted when comparing lower velocity fragment observations to predictions, all fell on the side of lower apparent cavity pressures existing in the event than were predicted. Several reasons for the existence of lower than critical pressure ratio inferred pressures in the cavity have already been discussed. No theoretical reasons for the existence of higher than predicted cavity pressures (other than three-dimensional flow effects) have been identified nor have any observations shown that higher than predicted cavity pressures occurred in the single abort which was available for detailed study. It was noted that the fragments which were clockwise from the LSC (North trajectory)

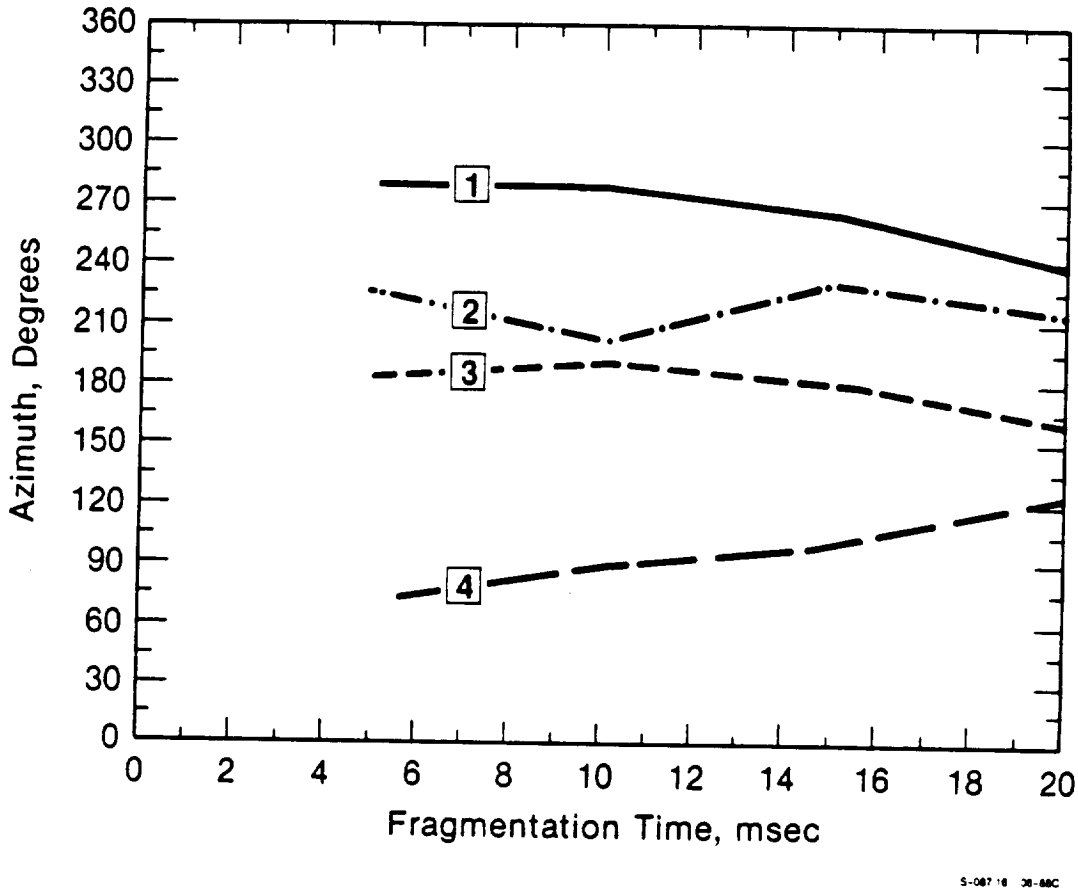

Figure 21. **Effect of Initial Location and Fragmentation Time on the Azimuth of Fragments Generated by a 34D-SRM Range Destruct Action at 10 Seconds MET (Squared numbers refer to fragments shown in Figure 11)**

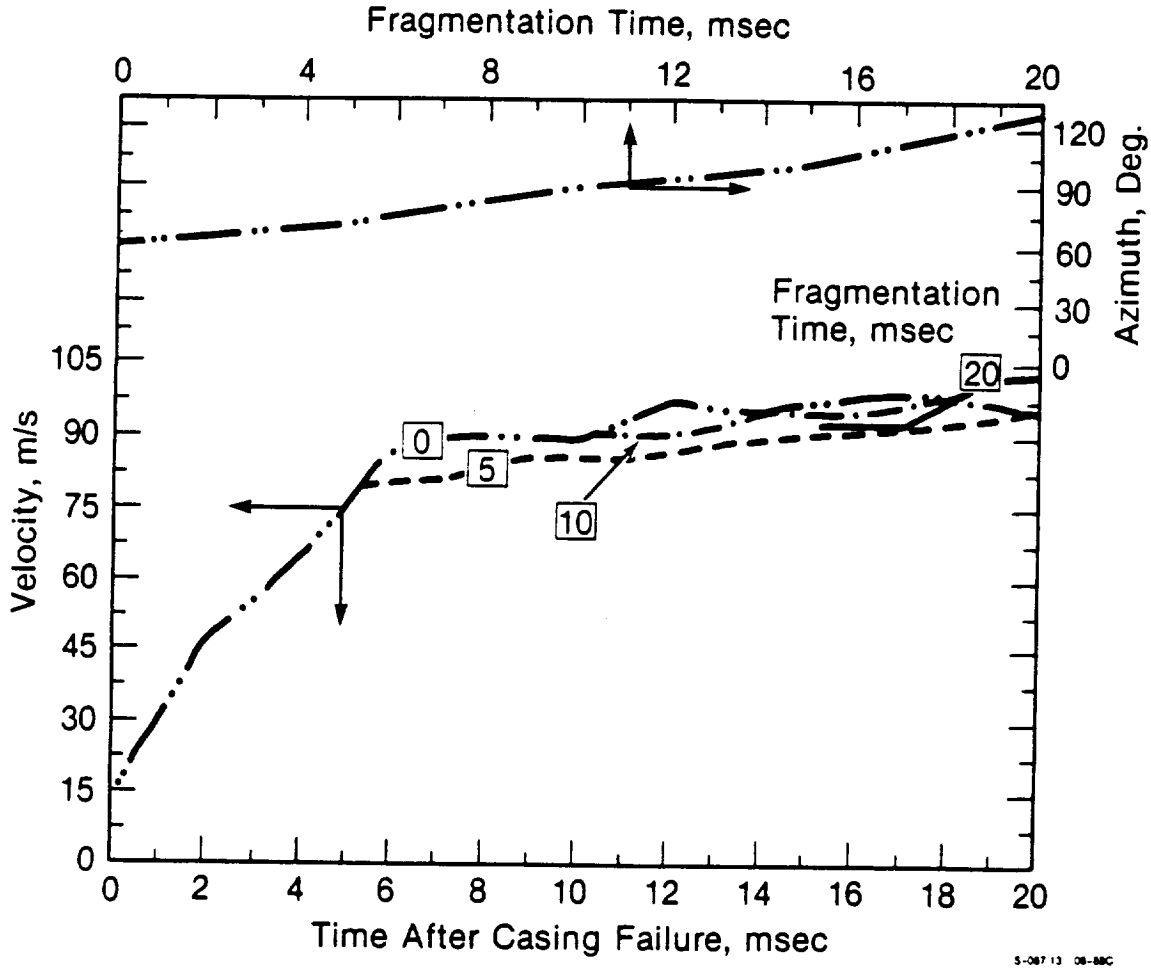

Figure 22. Effect of Fragmentation Time on the Velocity and Azimuth of the Highest Velocity 34D-SRM Fragments (Number 4, Fast Octants), shown in Figure 19

Table 3. Comparison of the Observed and Predicted Fragment Velocity and Azimuth Resulting From the Range Destruct of SRM-1 in the 34D-9 Event

Observations Based On T34D-9 Range Data					Predictions Based On Hydrocode Calculations					
Segment	Piece	Range (m)	Azimuth* (deg)	Velocity (m/s)	AZ* (deg)	FT† (ms)	VEL (m/s)	AZ* (deg)	FT† (ms)	VEL (m/s)
					Kp** = 0.8			Kp** = 1.0		
1	497	418	108	105	107	18	89	107	18	105
3	493	362	115	105	110	18	91	110	18	106
3	500	350	84	99	86	10	84	85	10	102
4	427	346	76	88	86	10	82	86	10	99
5	1564	356	−58	100	−78	8	98	−76	8	119
					Kp** = 0.2			Kp** = 0.4		
1	520	248	−86	56	−86	12	38	−86	12	59
	538	194	−56	39	−91	10	27	−91	10	41
2	480	162	71	30	91	10	27	91	10	41
4	484	251	128	53	109	18	45	109	18	59
	1077	133	−63	27	−91	10	29	−91	10	45
5/6	483	206	117	43	106	18	22	106	18	64

*Initial Casing Failure at 0 Degree

**Arbitrary Cavity-Pressure Reduction Factor Used to Match Observed Results[7]

†Fragmentation Time.

attained higher velocities than those which were counterclockwise from the LSC. The mechanism for producing short range and long range cutline fragments is probably related to the degree to which these casing fragments were in the lee of grain fragments and to the timing of the casing-grain debonding. These factors are statistical in nature and no attempts to infer mechanistic causal relations were made. The entire fragment velocity domain of the 34D-9 event could be captured using a 20 to 100 percent range for the cavity pressure forcing function shown in Figure 17. It should be noted that these same observed lower velocities (labeled short range in Table 2) can be predicted by assuming that the casing and PBAN grain do not debond and that they move as a single body (Figure 2). The agreement obtained between predictions and observations was considered sufficiently good to establish the efficacy of the modeling process, for use in generating an STS-SRM fragmentation statistical data base.

c. MODEL APPLICATION. A detailed model of the STS-SRM was prepared using the same early MET modeling process that was calibrated against the Titan 34D-9 event. The predicted[6] chamber pressure time-history for an STS-SRM is presented in Figure 23. The STS-SRM gas and grain characteristics are presented in Table 4. Additional characteristics of the STS-SRM are presented in Table 5.

The development of a typical assumed STS-SRM fragmentation pattern is shown in Figure 24. The sensitivity of the fragment geometry and velocity to fragmentation time is shown in Figure 25. Figure 25 is analogous to the 34D-9 results shown in Figure 20. Identical trends and slightly lower abso- lute values of velocity were noted between the STS-SRM and 34D-SRM fragments when using identical boundary assumptions. Figure 26 shows the sensitivity of fragment azimuths to casing fragmentation time. Figure 27 is a cross plot of the fast fragments (fragment 1) from Figure 25 as well as a restate- ment of the variation of fragment 1 azimuth as a function of fragmentation time. Figure 23 compares to Figure 19 of the 34D-9 calibration analysis.

Additional calculations for 10 second MET failures were performed at a number of assumed fragmentation times to create a statistical data base for the Shuttle Data Book. These

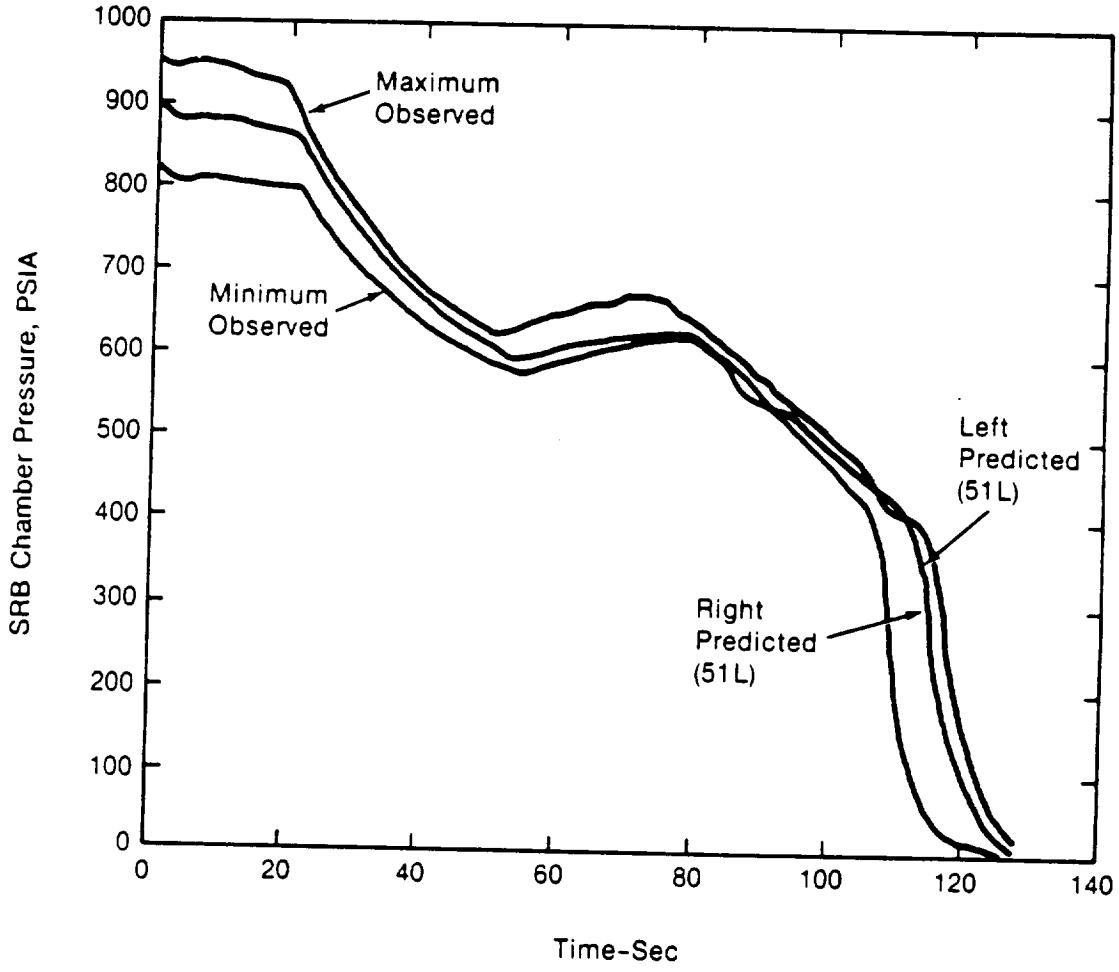

Figure 23. STS-SRM Chamber Pressure Experience[6]

Table 4. STS-SRM Propellant Characteristics[8]

Flight Time (sec)	Propellant Weight (lb)	Burn Radius (in)	Propellant Burn Area (in^2)	Chamber Volume (in^3)	Chamber Pressure (psia)	
					Head	Aft End
1	1,108,355	30.698	461336.0	4365466.0	831.5	759.5
6	1,051,639	32.605	477994.0	5258631.4	848.2	794.4
12	981,275	34.911	487578.0	6366725.8	850.1	809.3
18	909,343	37.224	495370.0	7499513.2	852.4	820.0
24	840,987	39.503	469380.0	8575985.7	771.9	747.5
30	781,382	41.707	440032.0	9514647.1	700.5	681.6
36	726,201	43.844	419440.0	10383639.2	644.7	629.7
42	673,831	45.919	400537.0	11208363.6	591.4	579.5
48	624,044	47.943	385567.0	11992410.9	556.9	547.2
54	575,407	49.937	382237.0	12758347.9	541.7	533.5
60	526,297	51.926	390886.0	13531733.7	548.1	540.7
66	476,384	53.928	396986.0	14317765.2	561.1	554.3
72	424,727	55.948	409223.0	15131261.3	577.6	571.5
78	370,760	57.986	421554.0	15981135.3	588.4	582.9
84	314,736	60.037	424782.0	16863403.0	597.6	592.7
90	258,294	62.099	432464.0	17752253.4	606.2	601.7
96	200,243	64.171	440387.0	18666442.4	615.3	611.2
102	143,571	66.239	425016.0	19558914.8	597.9	594.3
108	89,025	68.331	408811.0	20417906.9	564.5	561.4
110	71,584	69.019	400355.0	20692568.4	551.6	548.7
112	54,717	69.682	386063.0	20958190.4	537.1	534.3
114	39,054	70.329	383733.0	21204851.8	473.0	470.6
116	24,366	70.939	333787.0	21436158.9	382.8	380.9
118	13,310	71.489	262552.0	21610269.1	252.7	251.4
120	5,975	71.957	186429.0	21725781.0	149.0	148.3
122	2,383	72.312	69990.0	21782347.9	32.9	32.7
124	2,246	72.520	9093.0	21784505.4	6.7	6.6

Chamber Pressure (psia)	Chamber Gas Temperature (°K)	Chamber Gas Density (RHO, g/cc)
5	2911	3.8226-5
15	3027	1.1170-4
25	3081	1.8399-4
50	3154	3.6239-4
100	3226	7.1434-4
150	3267	1.0629-3
200	3295	1.4094-3
250	3317	1.7545-3
300	3334	2.0985-3
350	3349	2.4416-3
400	3361	2.7840-3
450	3372	3.1257-3
500	3382	3.4669-3
550	3390	3.8076-3
600	3398	4.1479-3
650	3405	4.4878-3
700	3411	4.8274-3
750	3417	5.1667-3
800	3423	5.5056-3
850	3428	5.8443-3
900	3433	6.1828-3
950	3437	6.5211-3
1000	3442	6.8591-3

Table 5. Properties of Materials Used in the STS-SRM

Material[a]	Casing	Grain (Solid)	Grain (Reaction Gas)
Type	D6A Steel	PBAN	PBAN
Equation of State			
Polynominal			
Young's Modulus, kbar	—	0.0455[d]-0.121[e]	
Bulk Modulus, kbar	1670.	12.6[d]-33.5	—
Poissions' Ratio	0.3	0.4994	—
Reference Density (ρ_o), gm/cc	7.86	1.775[a]	—
Gamma γ[b]	—	—	1.142
Specific Internal Energy, eu[b][c]	—	—	0.0672
Reference Density (ρ_o), gm/cc[b]	—	—	0.00571
Yield Model	Von Mises	Von Mises	—
Shear Modulus , kbar	816	0.0126[d]-0.0403	—
Yield Strength, kbar	12.9	0.0087[d]-0.0483	—
Spall Strength, kbar	1000.	100.	—
Elongation to Failure, %	10.	26.-52.	—
Cylinder			
Thickness, cm	1.22	~115.	—
Height, cm	410.7	~400.	—
Diameter, cm	365.8	363.	—
Membrane Mass, Kg	330	—	—
Joint Mass Averaged Over Cylinder, kg	53.	—	—
Total Cylinder Mass, kg	383.	—	—
Fwd Cylinder-10 Sec MET			
PBAN, kg	—	—	—
Insulation Averaged Over Cylinder, kg	23.5	—	—
Total FWD Cylinder, kg	406	—	—
Fwd Cylinder-110 Sec			
PBAN, kg	—	422.2	—
Insulation Averaged Over Cylinder, kg	17.2	—	—
Total Cylinder Mass, Kg	822.	—	—
Aft Cylinder-110 Sec MET			
PBAN, kg	67.8	68.6	—
Insulation Averaged Over Cylinder, kg	46.1	—	—
Total Aft Cylinder, kg	500.	—	—

[a] The rubber inhibitor is treated as having the same physical response as solid grain. The PBAN grain ρ_o is adjusted from 1.76 gm/cc to account for the presence of the inhibitor.

[b] Varies with burn time. See Figure 13 and Table 4 for typical geometry and pressure response.

[c] One eu is 10^{12} ergs.

[d] At 75°F. Thiokol Data[13].

[e] Results of dogbone test at elevated strain rates. UTC Data[1]

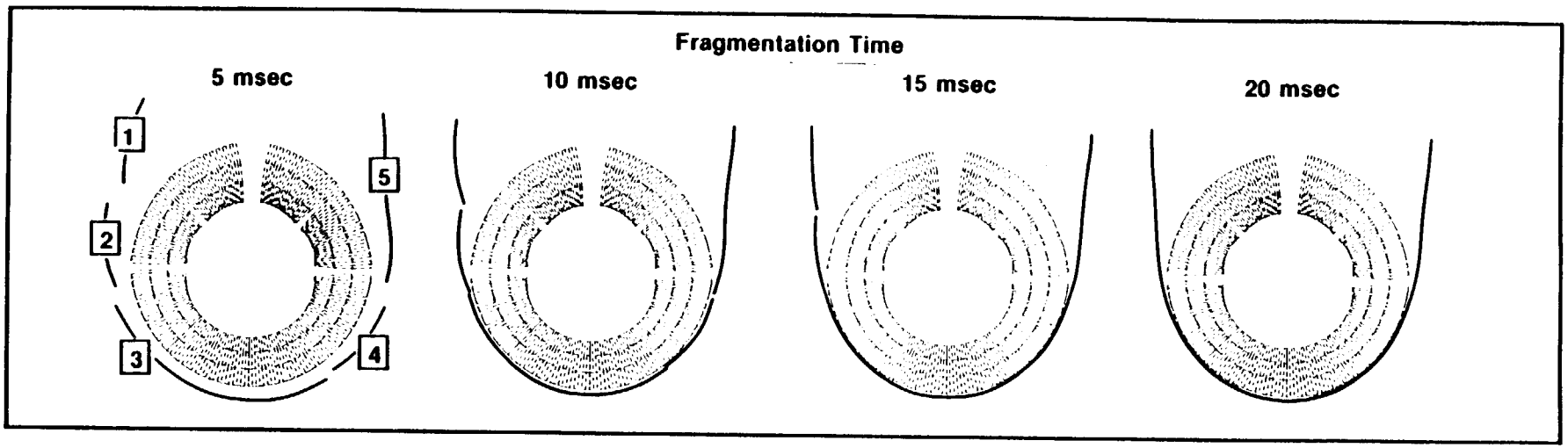

Figure 24. STS-SRM Casing Geometry for Four Assumed Fragmentation Times 20 msec After a Range Destruct Action at 10 Seconds MET

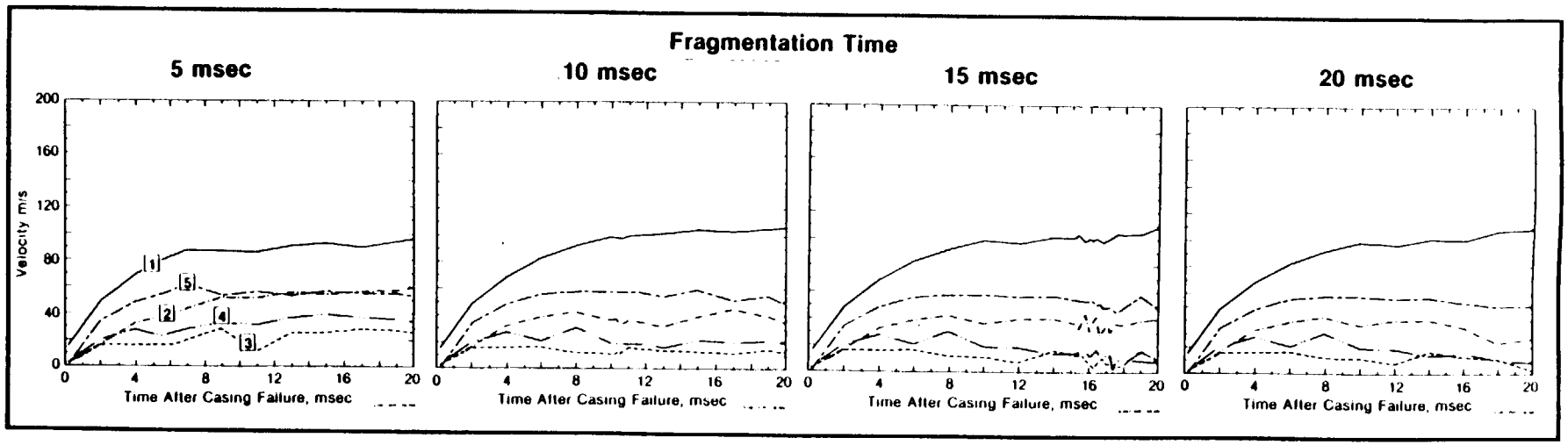

Figure 25. Time-History of Fragment Velocities Resulting From the Range Destruction of a STS-SRM for Four Assumed Fragmentation Times at 10 Seconds MET (Squared numbers refer to fragments shown in Figure 24)

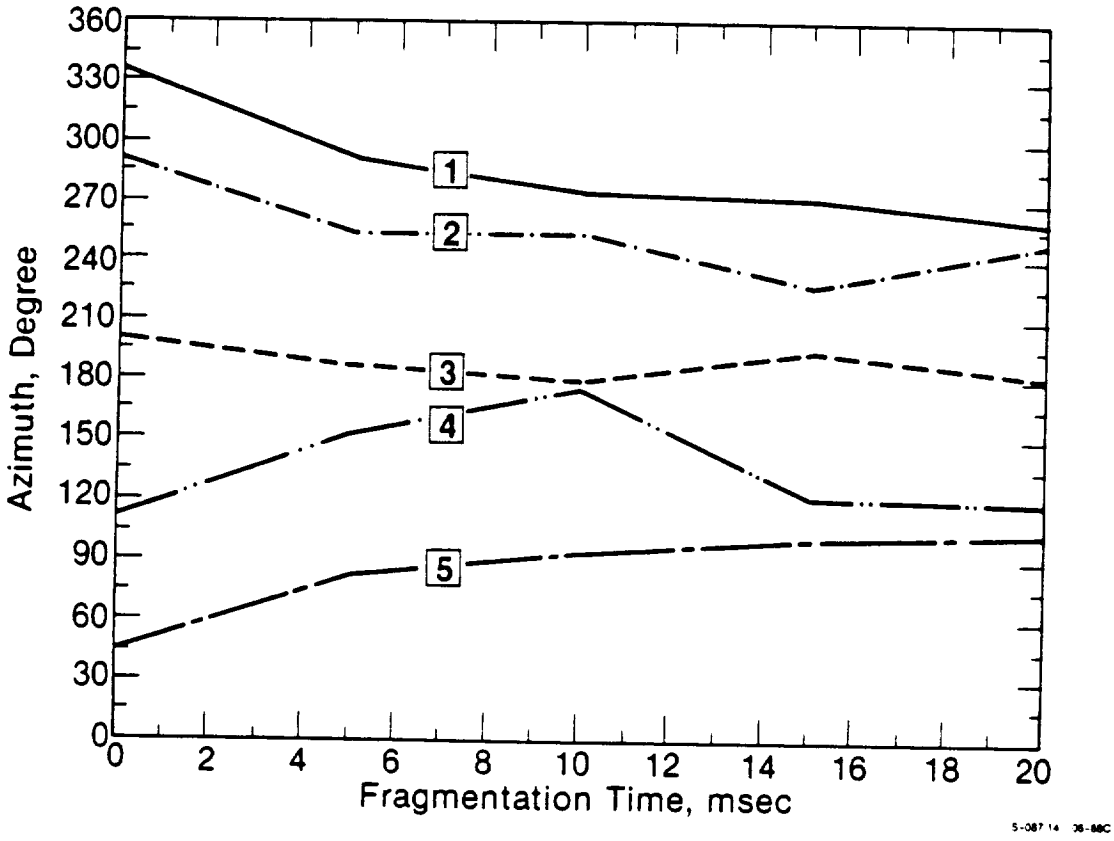

Figure 26. **Effect of Initial Location and Fragmentation Time on the Azimuth of Fragments Generated by a STS-SRM Range Destruct Action at 10 Seconds MET (Squared numbers refer to fragments shown in Figure 24)**

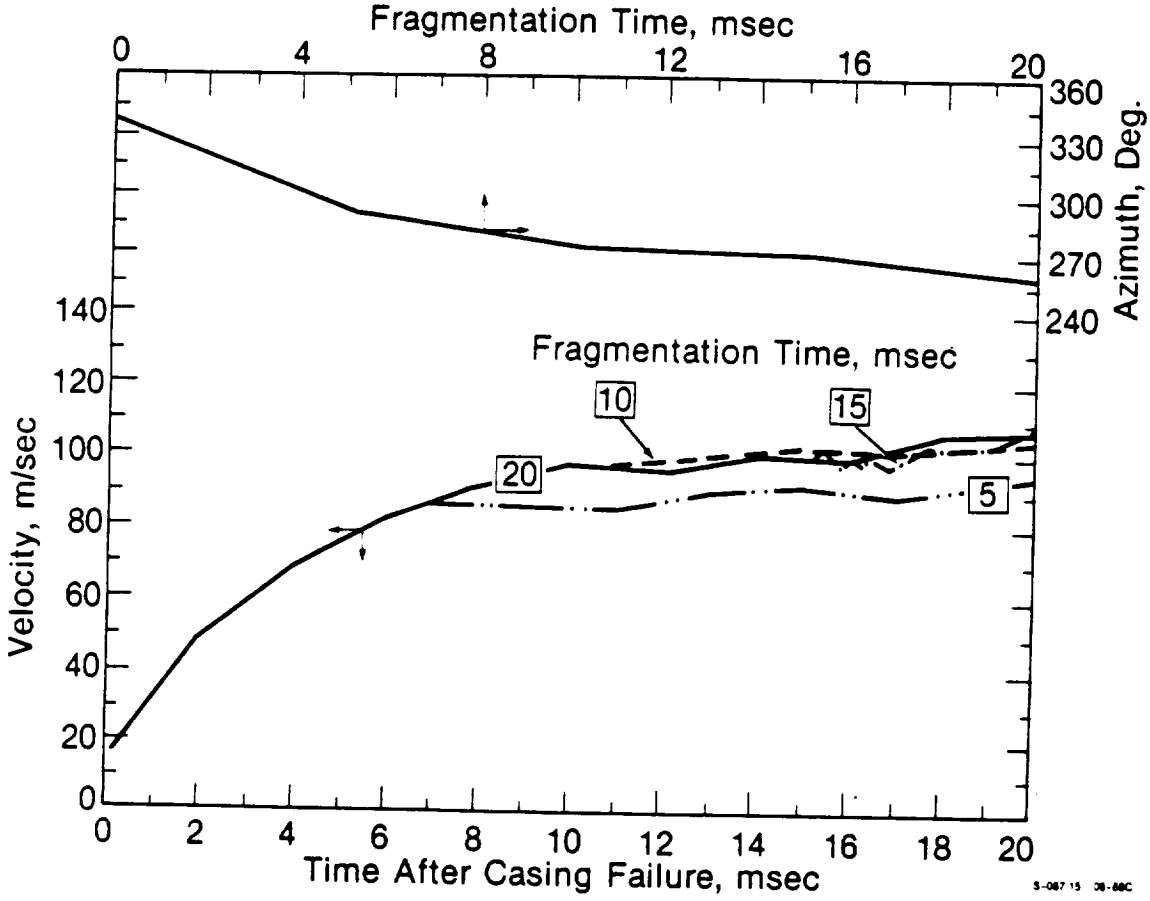

Figure 27. Effect of Fragmentation Time on the Velocity and Azimuth of the Highest Velocity STS-SRM Fragments (Number 1, Fast Octants) Shown in Figure 24

results were transmitted to JPL and GE on magnetic tape and are full documented and reproduced in Appendix A.

Stress boundary calculations using the thick grain models were performed at 84 sec MET for a number of fragmentation times to create a statistical data base for the Shuttle Data Book. The results were similar to those shown above. The details of these calculations are not presented here but they are fully documented in Appendix A.

2. Late MET Failures (Thin Grain Models)

Late MET is defined as the time at which the grain has burned down to a thickness small enough such that its extant inertia and stored strain energy allow the grain to track the circumferential "twang" of the casing. Under these conditions no debonding occurs, and no cavity between the grain and casing is formed. It is much less difficult to model late MET failures than early MET failures. In late MET failures the fragmentation forcing function is generated by simply applying the chamber pressure to the inner grain surface.

A number of stress boundary calculations were performed to develop the 110 sec MET failure data base. These calculations were performed using the aft-center segment as typical of the STS-SRM. At 110 sec MET, the forward cylinder of the aft-center segment has a maximum of about 6.5 cm of PBAN remaining. The aft cylinder of the aft-center segment has almost all fuel consumed. This difference in grain thickness is due to the initial taper of the grain (see Figure 13) and its approximately constant recession rate during burning. The mass of the bonded fuel remaining has a large effect on the predicted velocity of the SRM fragments. Calculations were performed to determine the velocity and azimuth of fragments originating in an aft cylinder of an aft-center segment. These fragments and those originating in the SRM dome and star grain segment will have the highest velocities in late MET aborts since they have the lowest areal density and the chamber pressure acts directly upon them. Peak velocities somewhat higher than 200 m/s were predicted for these fragments. A summary of the material characteristics used for the late MET stress boundary calculations

was presented in Table 5. The data base generated using these input parameters and the stress boundary methods discussed previously is presented in Appendix A.

The material presented in Appendix A is used as input to a Monte Carlo calculation which randomizes, among other things, SRM casing failure MET and fragmentation time. Before they can be used to predict a threat at the RTG location, the momenta implied in the tables presented in Appendix A must be corrected for any chamber impulse remaining at the randomly selected fragmentation time. This correction was performed using a post-processing code developed by Jaffe[4] and transferred to GE. The authors were requested to calibrate this post-processor by performing a series of 110 sec MET calculations using four assumed fragmentation times. These were fully defined coupled Eulerian-Lagrangian calculations of the type which had been used to develop the flow field basis for Figure 17.

A 110 sec MET casing failure Eulerian-Lagrangian coupled model of an STS-SRM forward cylinder of an aft-center segment is shown in Figure 28. The fragmentation approximates that of a segment observed in the 51L event[5]. Plots of predicted velocity as a function of time after initial failure are shown in Figure 29. Examination of Figure 29 shows that the smaller of the fragments (fragment 1) adjacent to the failure site has the highest velocity of any of the segment fragments. Also, it is seen that the magnitude of this velocity is much more sensitive to casing fragmentation time than was the case for early MET failure. Examination of Figure 30 reveals the expected sensitivity of the azimuth of the fast fragments to the casing fragmentation time. The fastest fragments shown in Figure 30 are cross plotted on Figure 31 to show the sensitivity of maximum fragment velocity to casing fragmentation time. It is interesting to note that the velocity of the fastest fragments increases by 25 percent when comparing late MET events with break times varying from 5 msec to 20 msec. Similar comparisons for early MET failures resulted in velocity increases of less than 10 percent. Plots of the chamber-pressure time-history, at a fixed Eulerian location just inside the center of fragment 1, for the four assumed fragmentation times are shown in Figure 32. The original prediction of STS-SRM chamber-pressure time-history which was shown in Figure 3 is repeated in Figure 32 for reference. Examination of Figure 32 shows a clear trend of chamber pressure decay. The earlier the fragmentation time, the faster the chamber pressure decays.

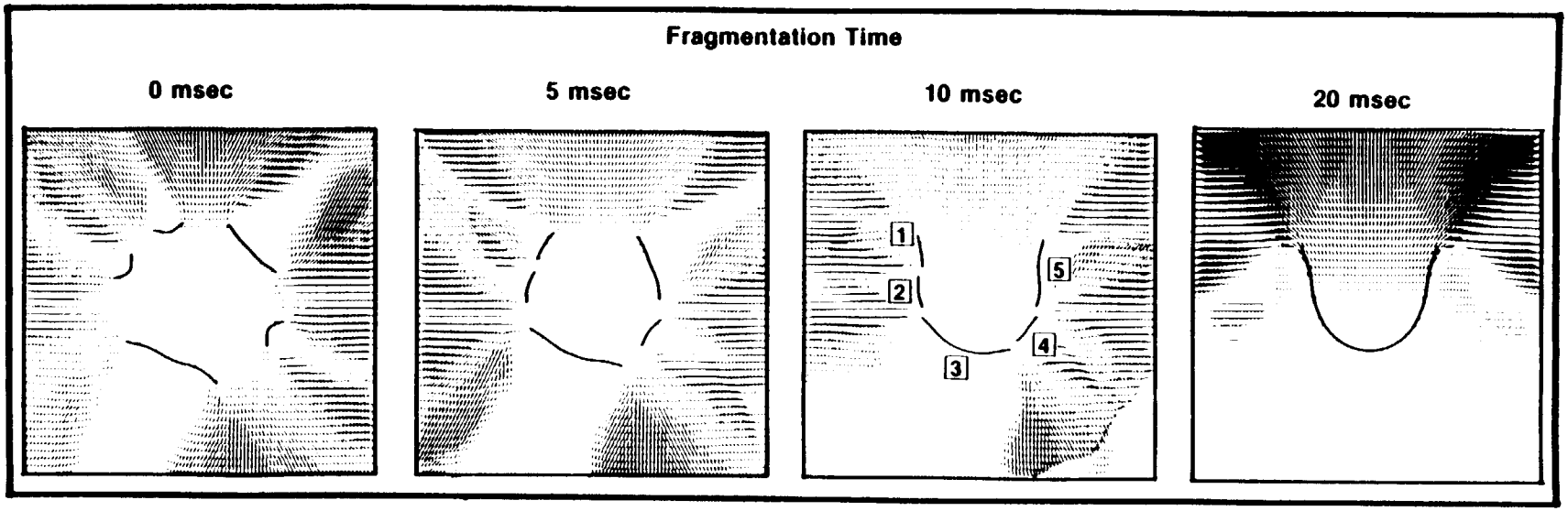

Figure 28. STS-SRM Casing Geometry for Four Assumed Fragmentation Times 20 msec After a Range Destruct Induced Casing Failure

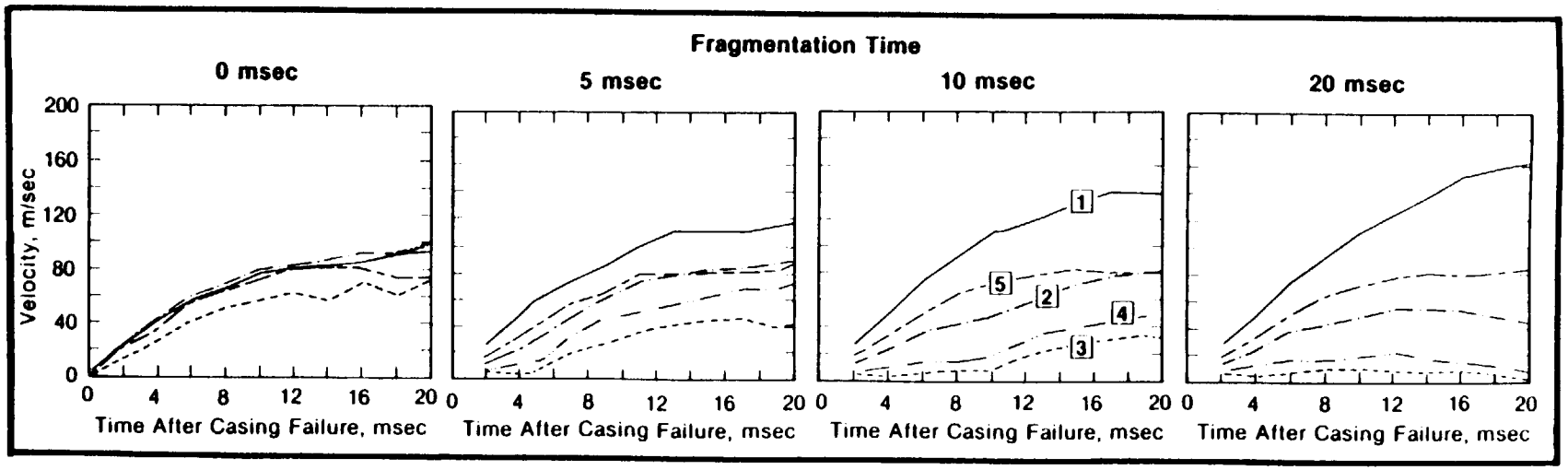

Figure 29. Time-History of Fragment Velocities Resulting from the Range Destruct Induced Failure of a STS-SRM for Four Assumed Fragmentation Times

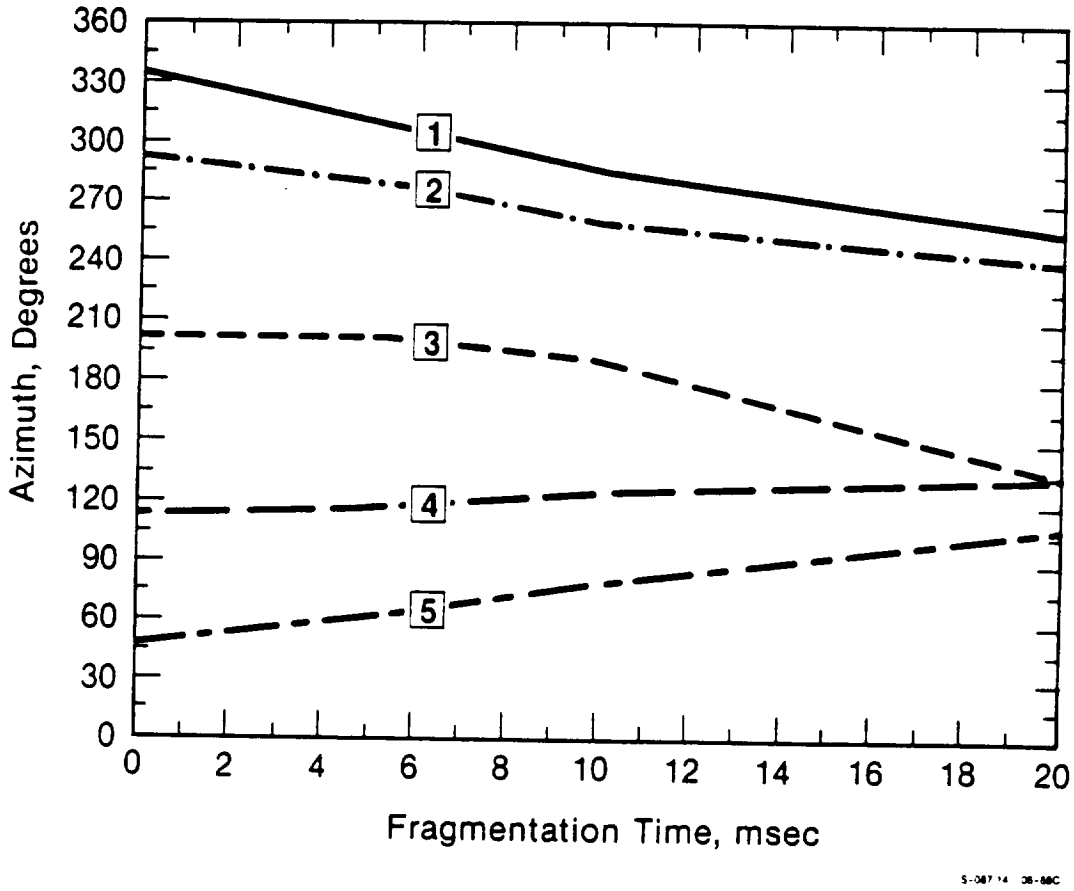

Figure 30. **Effect of Initial Location and Fragmentation Time on the Azimuth of Fragments Generated by a STS-SRM Range Destruct Action at 110 Seconds MET (Squared numbers refer to fragments shown in Figure 28)**

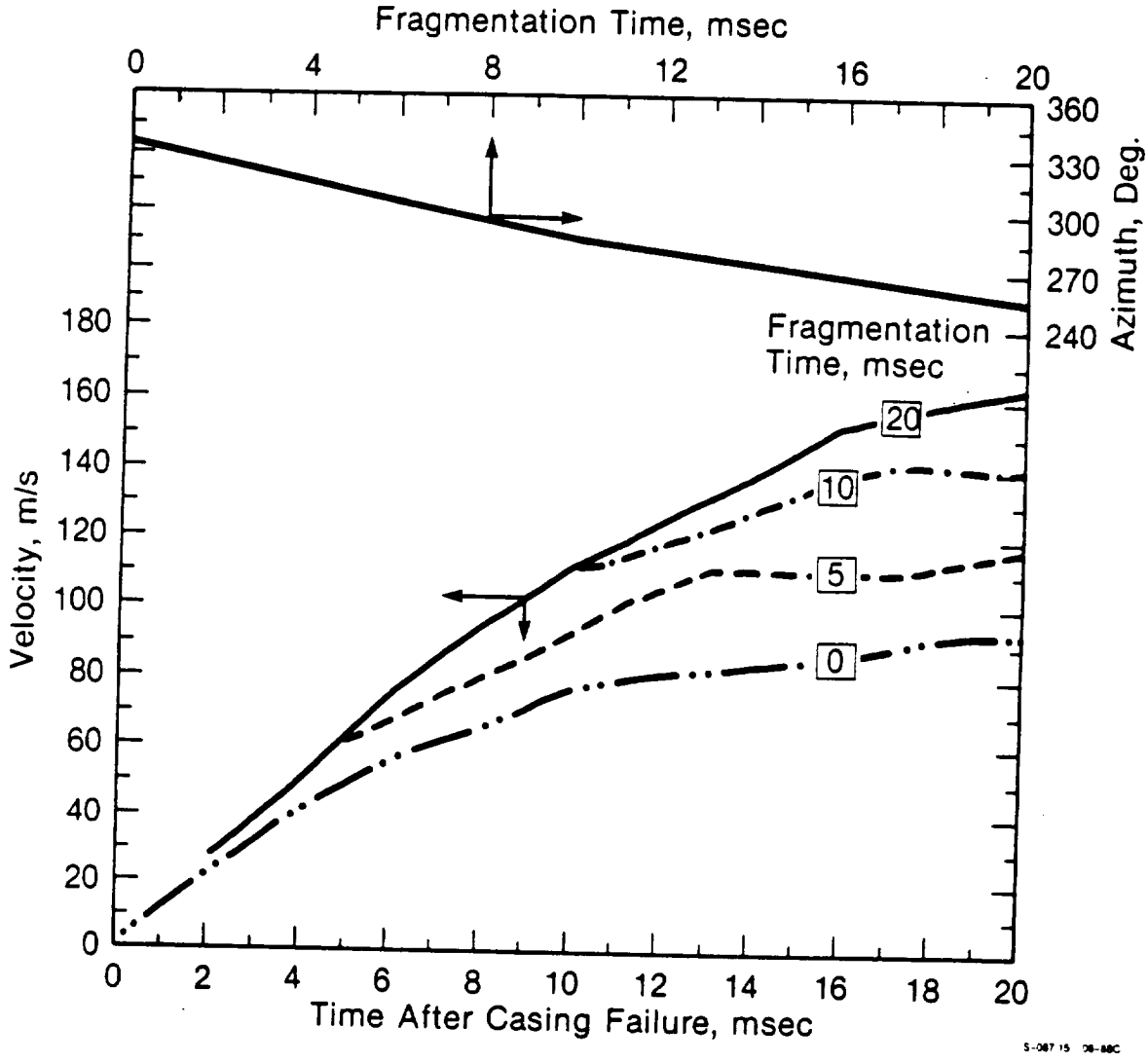

Figure 31. Effect of Fragmentation Time on the Velocity and Azimuth of the Highest Velocity STS-SRM Fragments (Number 1, Fast Octants) Shown in Figure 28

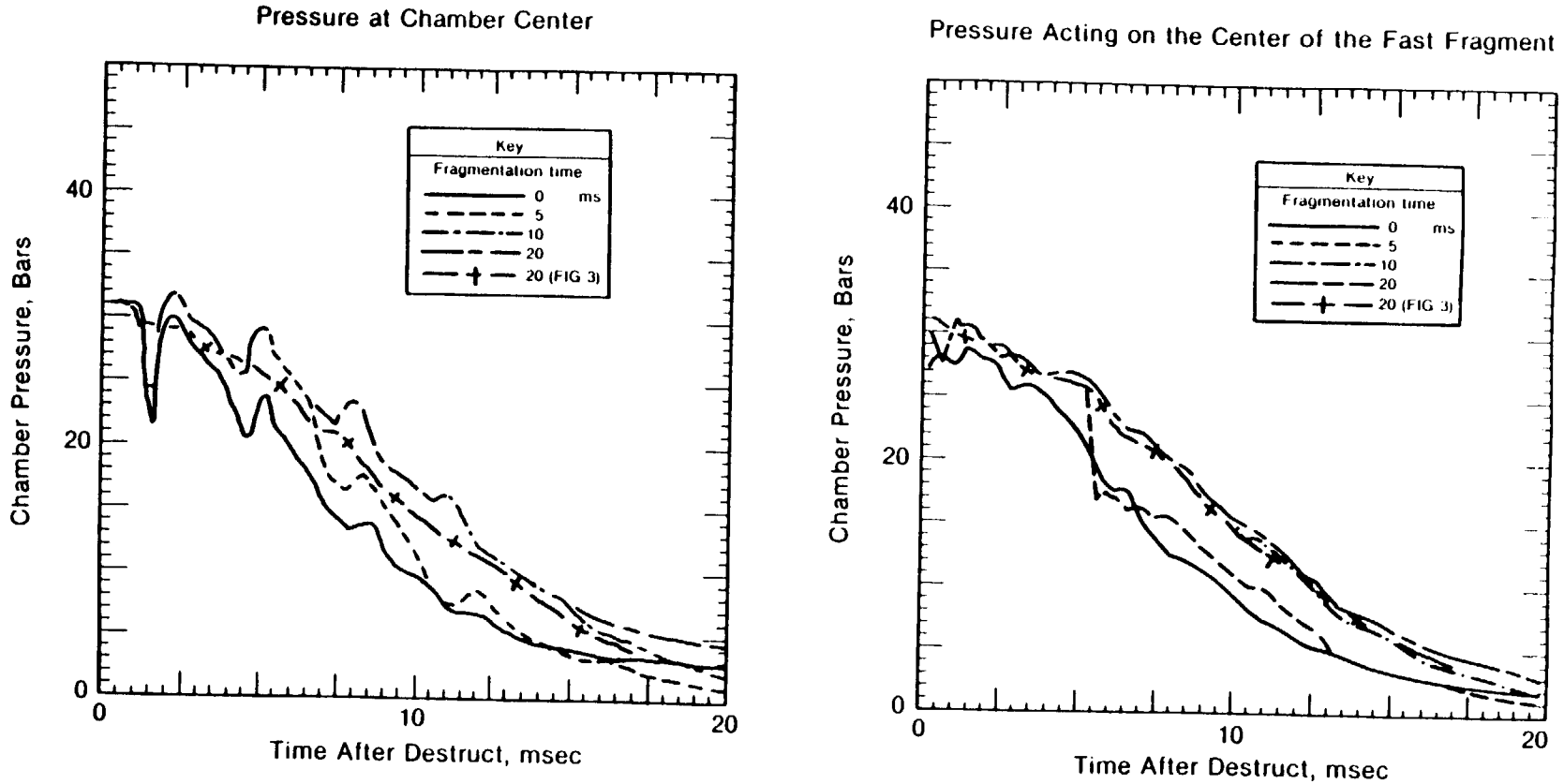

Figure 32. Time-History of STS-SRM Chamber Pressure at Two Locations and Various Casing Fragmentation Times Following a Range Destruct at 110 Seconds MET

Note that the *integrals* of all of the fragmentation time time-history curves (impulse) shown in Figure 32 are lower than the integral of the time-history used to develop the Figure 17 data base. This means that the fragment velocities used in the Shuttle Data Book may be slightly conservative. A comparison of the velocity predictions shown in Figure 29 to those made using Jaffe's post processing code showed good agreement.

The late MET data base showed good agreement with the 51L data reduction performed by Parker[9] and with Kolp's[5] observations. Given this good late MET agreement and the good early MET agreement inferred from the Titan 34D-9 results, the authors consider the range destruct fragment data base to be well calibrated and reliable for use as input into the Galileo FSAR threat assessment.

B. SRM Random Failures

Range destruct induced SRM fragmentation produces essentially the same fragment velocity distribution for each SRM segment. Random failure induced SRM fragmentation produces fragment velocity distributions which are dependent upon the segment-of-interest's stack location and the stack location of the randomly failed segment. Preliminary evaluations of 34D-9 SRM-2 indicated that the upper segment fragments had a lower average velocity than did those of the range destructed SRM-1. These considerations greatly complicated the analytical modeling of the random failure of SRM segments. These complications were brought about by the need to account for longitudinal flow (z-flow) in the gas flow-field modeling.

Longitudinal flow of the gas stored in the SRM chamber has two effects. First, this flow tends to increase the impulse available to accelerate fragments generated in the randomly failed segment. Second, by reducing the chamber pressure along the longitudinal axis of the SRM, the existence of this flow tends to reduce the velocity of fragments generated from those segments which were initially sound. In general, the failure of segments other than the randomly failed segment occurs because propagating cracks produce stress concentrations in structures which are otherwise sound. If the crack propagation rate is slow enough, segments

at longitudinal positions distant from the failed segment may have their chamber pressure reduced by longitudinal flow below their failure threshold before a significant stress riser appears at the segment boundary. In this case the segment will not fragment.

Axisymmetrical models of the Titan 34D-SRM and STS-SRM were generated to test the sensitivity of the temporal variation in the longitudinal chamber pressure distribution to various crack propagation rates. The Titan 34D-SRM model was divided into five segments (nine for the STS). A grid plot of the Titan 34D-9 axisymmetrical calibration model and grid plots of the STS-SRM models used at 10, 84 and 110 seconds MET are shown in Figure 33. Each segment of each of these models is fitted with a "slide valve." This valve is an analytical artifact to allow the variable rate of radial outflow of gas which is required for a two-dimensional simulation of the sequential failure of each SRM segment.

The change in available gas radial flow area with time was inferred from the initial coupled calculation results presented in Figure 2. The variation with time of the x-position of the edge of the last node of the Titan 34D-9 SRM casing model is shown in Figure 34. Knowing the location of this boundary in space and time, one may calculate the temporal variation of flow area and the rate of change of the flow area through which the chamber gas may exit the casing. Since the diameter of the casing is known, this information may be used to calculate a "slide valve" velocity profile which will produce an identical rate of change of flow area in the axisymmetrical model. Each segment of the SRM was fitted with a "slide valve" (5 for the 34D-SRM and 9 for the STS-SRM). The delay time between the serial opening of the slide valves is related to the segment transit time for the crack (i.e. segment height and crack propagation rate). Typical Titan 34D and STS-SRM model valve velocity-time schedules are presented in Table 6.

The variation of the x-position of the edge of the last node of the STS-SRM casing model is shown in Figure 35 for three METs. The rate at which these valves opened was determined in the same manner as was described above for the Titan 34D-9 case. The time at which valve opening began was determined by the longitudinal position of the subject segment in the stack, the crack propagation rate, and the crack segment-transit time, since all segments

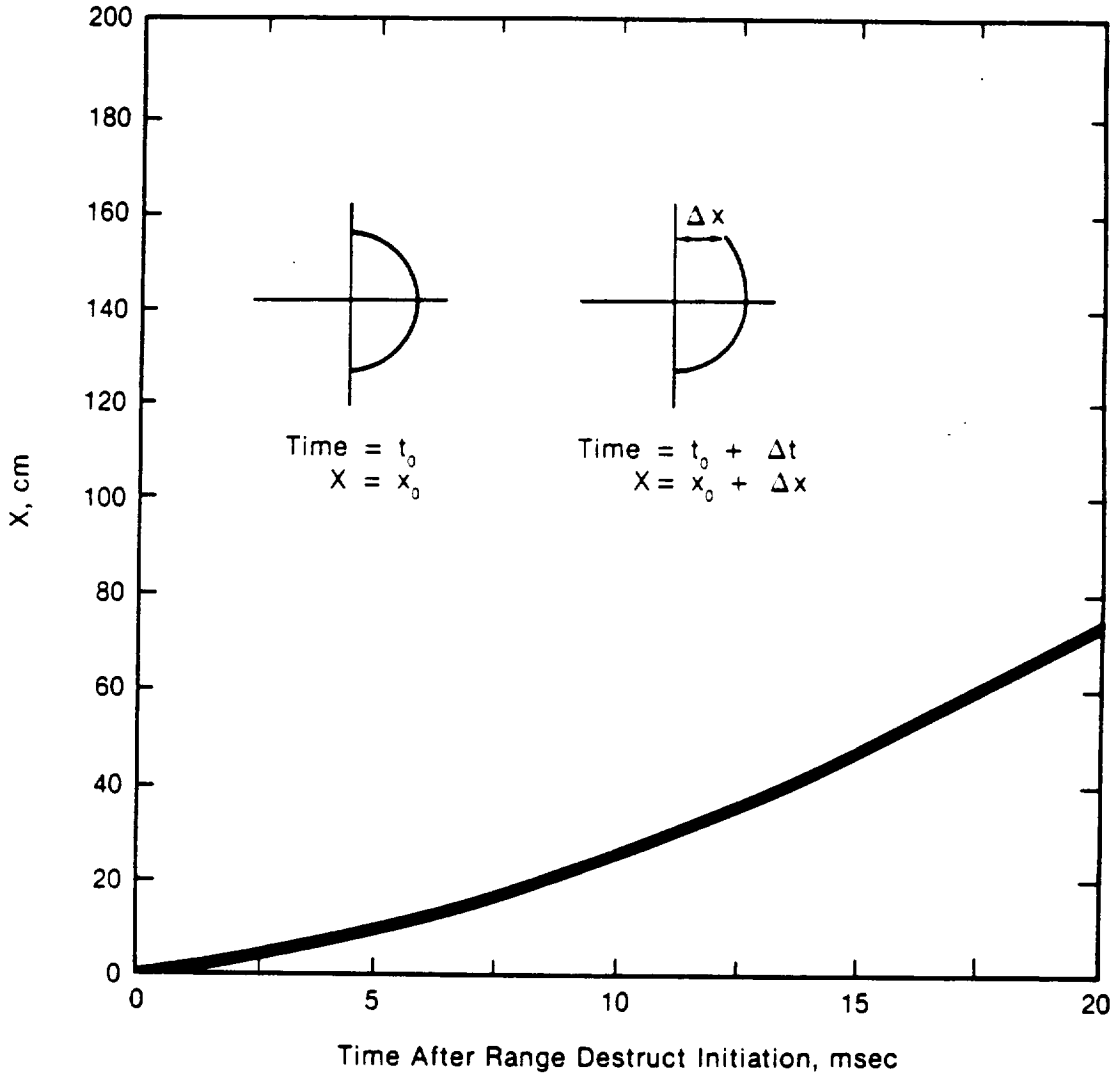

Figure 34. Time History of TITAN 34D Casing-Edge X-Location Following a Range Destruct Action at 10 Seconds MET

Table 6. Valve Velocities Used to Generate Radial Outflow From the Axisymmetrical SRM-Random-Failure Model

Time After Initial Failure	Valve Velocity Profile[a]			
	34D at 10 sec MET	STS at 10 sec MET	STS at 84 sec MET	STS at 110 sec MET
msec	cm/msec	cm/msec	cm/msec	cm/msec
5	1.0	1.4	2.0	3.5
10	2.1	2.0	4.0	7.0
15	2.8	3.0	6.0	9.1
20	3.4	3.6	6.1	10.5

[a]All 34D-SRM Segments are identical. The values shown for the STS-SRM are for Segments 4 through 9. Length-corrected tables were used for cylinders in the STS aft segment.

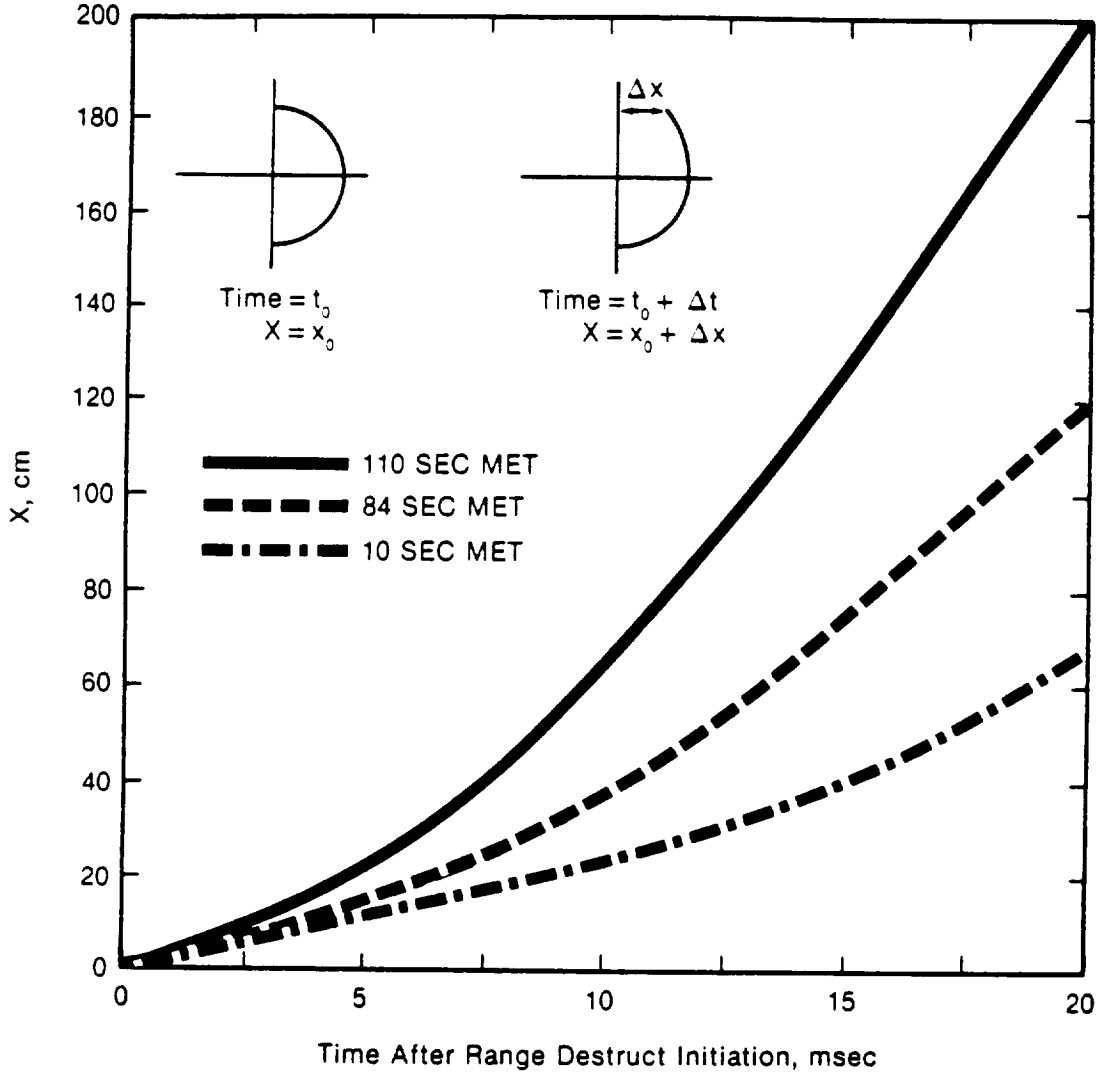

Figure 35. Time History of STS Casing-Edge X-Location Following a Range Destruct Action at Three Failure METs

were not of equal length. Typical valve delay-time-before-opening schedules for the 34D and STS-SRM are shown in Table 7. For the Titan 34D-9 event, a delay time to begin radial flow from each segment was selected using crack propagation rates of 534 and 320 m/s. The results of calculations employing all of the devices discussed above are presented in Figure 36. Examination of this figure shows that upper-segment-pressure reductions of a factor of two can occur prior to casing fragmentation for these crack propagation rates.

The impulse available to accelerate fragments from an early-MET segment failure can be obtained by correcting the integral of the relevant pressure-time-history curve shown in Figure 36 by the normalization factor shown in Figure 17. The ratio of these values of impulse to a Figure 17 corrected integral of the relevant Figure 3 pressure-time-history curve will provide a basis for assessing the effects of z-flow on fragment velocity in SRM random failure events. Nance, et. al.[7] noted that the peak value of fragment range observed from each segment of the randomly-failed 34D-9-SRM-2 decreased as the longitudinal distance from the initially failed segment (Segment 1) increased. A comparison of impulse ratio calculated for two crack propagation rates to the impulse ratio inferred from fragment peak range data is shown in Figure 37. The agreement shown between the values calculated for a crack propagation rate of 320 m/s and the observed results was considered acceptable to validate the modeling techniques.

Parker[10] has observed that the crack propagation rate for an STS-SRM would be expected to be higher than that observed for a Titan 34D. This observation is based on his judgement that the 34D flange is more robust than the STS-SRM flange and that it is not fitted with an LSC. Because of this concern, the results of the calculations presented for three mission elapsed times in Figure 38 are based on a crack propagation rate of 534 m/s. A factor of two head-to-nozzle pressure variation is seen in all of these cases. A typical STS-SRM longitudinal pressure distribution 57.4 msec after a 110 seconds MET random failure had occurred in segment 1 is shown in Figure 39.

The model used to generate the 110 sec MET pressure-time-history shown in Figure 38 was also used to generate a z-flow argument into a late MET x-y translational symmetry

Table 7. Delay Times Used to Propagate Serial Segment Failures in the Axisymmetrical SRM-Random-Failure Models

Crack Arrival[a] at Aft Boundry of:	320 m/s	534 m/s	
	34D Segment Boundary Crack-Arrival Time	34D Segment-Boundary Crack-Arrival Time	STS Segment-Boundary Crack-Arrival Time
	msec	msec	msec
Segment 2	10.	6.	6.2
Segment 3	20.	12.	12.8
Segment 4	30.	18.	15.8
Segment 5	40.	24.	23.5
Segment 6	—	—	31.2
Segment 7	—	—	38.9
Segment 8	—	—	46.6
Segment 9	—	—	54.3

S-087 52 07-88C

[a]Random failure is assumed to occur in Segment 1 in all cases.

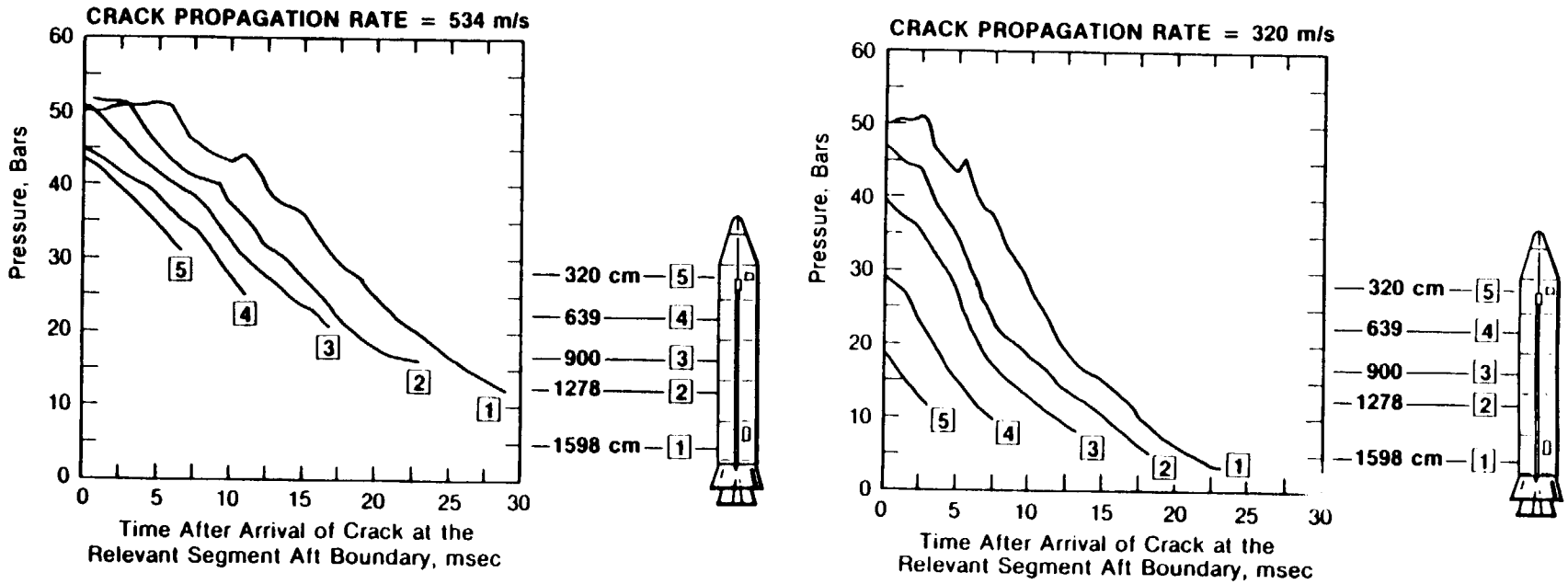

Figure 36. Time-History of the Pressure at Five Longitudinal Distances From the 34D-SRM Head After Random Failure in Segment 1 at 10 Seconds MET

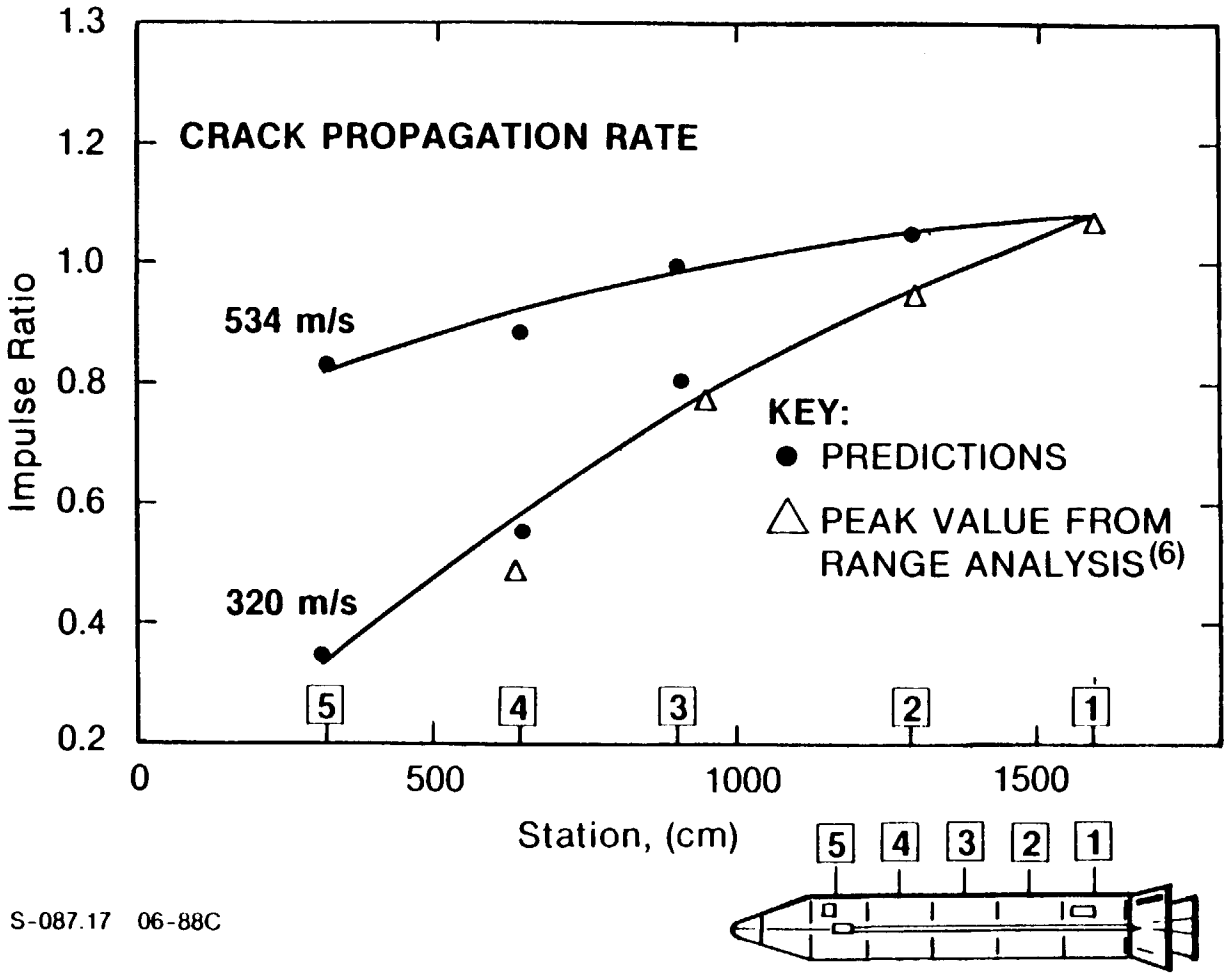

Figure 37. Correlation of Predicted and Observed Results From the 34D-9 SRM Random Failure

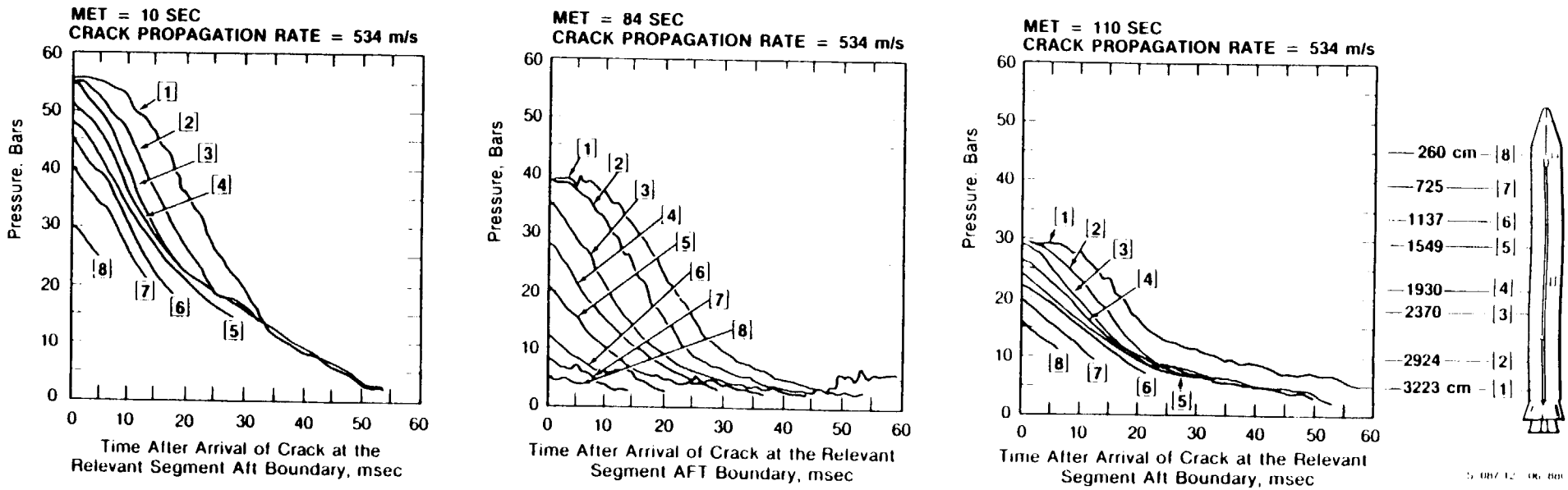

Figure 38. Comparison of Time-History of the Chamber Pressure at Eight Longitudinal Distances From the STS-SRM Head End After a Random Failure in the Aft Segment at a MET of 10 Seconds, 84 Seconds and 110 Seconds

Contours are Isobars.

Figure 39. **Longitudinal Pressure Distribution in an STS-SRM 57.5 msec After a Random Casing Failure Occurred in Segment 1 at 110 Seconds MET**

model. This model was used as a check on the overall efficacy of the predictive process. The flow field and fragment geometry predictions for the randomly failed forward cylinder of an aft-center segment of an STS-SRM at 110 sec MET are presented in Figure 40. Fragment velocities resulting from this same event are shown in Figure 41.

Comparison of these results to the range destruct cases discussed previously shows that at late MET, the randomly failed segment will produce fragments which, depending upon fragmentation time, have approximately three to seven percent higher velocity than will occur in range destruct cases. Concurrently, randomly failed SRM segments which are considerably displaced from the initially failed segment will have considerably less impulse to accelerate fragments than will range destructed segments. In the case of an STS-SRM at 110 sec MET, this reduction could be a factor of two even when using a high crack propagation rate.

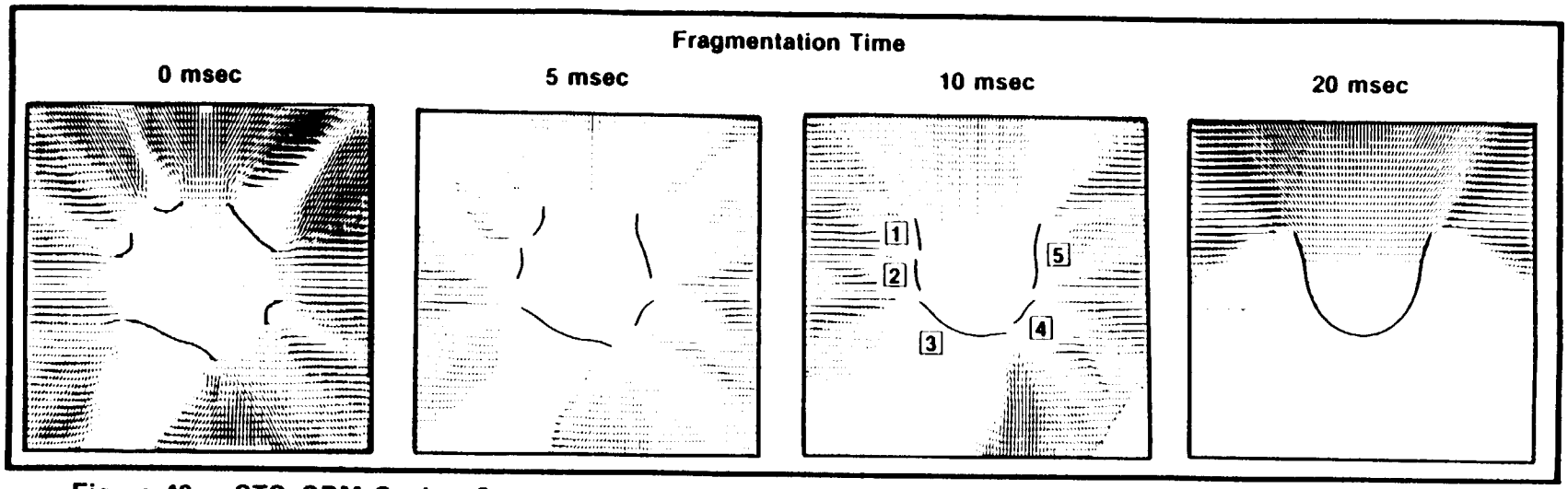

Figure 40. STS-SRM Casing Geometry for Four Assumed Fragmentation Times 20 msec After a Random Casing Failure

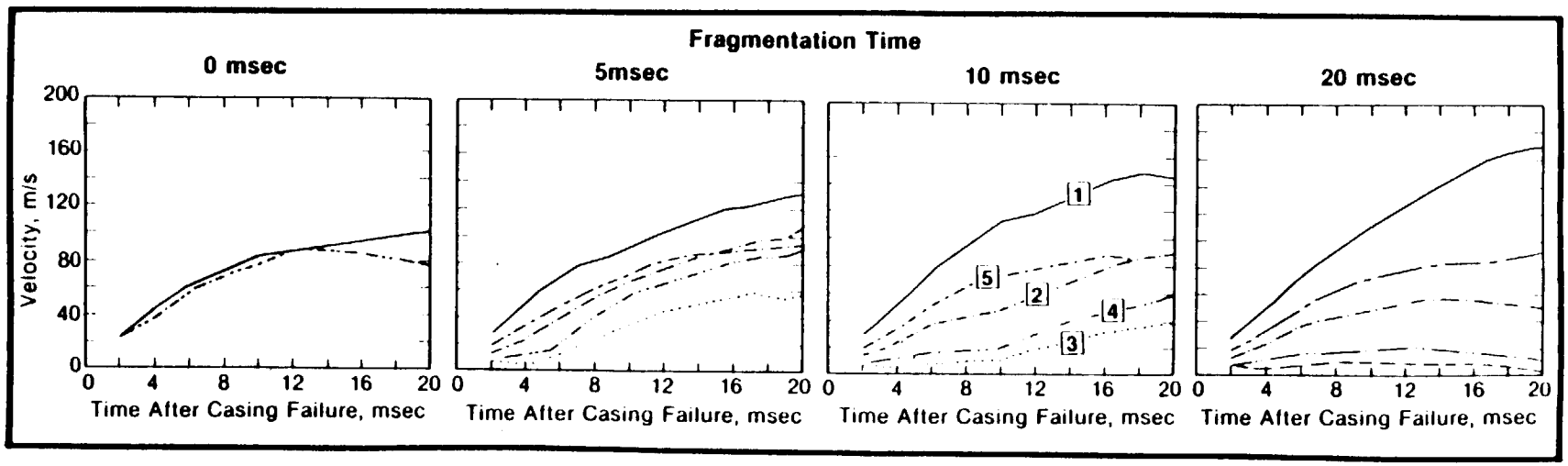

Figure 41. Time-History of Fragment Velocities Resulting From the Random Failure of a STS-SRM for Four Assumed Fragmentation Times at 110 Seconds MET (Squared numbers refer to fragments shown in Figure 40)

III. CONCLUSIONS

Results obtained using the analytical methods described in this report showed good agreement between predictions and observations for two specific events. It was shown that these methods have good potential for use in predicting the fragmentation process of a number of generically similar casing systems. It was concluded that coupled Eulerian-Lagrangian calculational methods of the type described in this report provide a powerful tool for predicting SRM casing fragmentation response.

IV. REFERENCES

(1) Backlund, Stan. Personal Communication. United Technology Corporation, October, 1987.

(2) Jaffe, Peter. Personal Communication. Jet Propulsion Laboratory, Pasadena, California, September, 1987.

(3) Ibid, December, 1987.

(4) Ibid, December, 1987.

(5) Kolp, G.F., Lyle, J.B. A Metric Analysis of the Challenger Accident. AIAA Paper 88-0570, Reno, Nevada, January 1988.

(6) Moorehead, Robert W, Chairman, et. al. JSC-STS 51-L Integrated Report, JSC-22152, Vol. 2, Figure 2.3.1.2-2. Houston, Texas, April, 1986.

(7) Nance, William, L. Garnholz, J. diPol. Personal Communication. RDA, Marina Del Rey, California.
K. Aaron, J. Cork, P. Jaffe, G. Spitale. Personal Communication. Jet Propulsion Laboratory, Pasadena, California, September, 1987.

(8) NSWC TR 80-417. Taken from memorandum from J.A. Roach (MSFC/NASA-EL-42, Huntsville, AL) to J. Petes (NSWC/WOL-WR-15, Silver Spring, MD) with subject title: "Closing of Action Items Resulting from NSWC and MSFC Meeting of July 17, 1975."

(9) Parker, Lloyd. Personal Communication. RTI, Cocoa Beach, Florida, December, 1987.

(10) Ibid, March, 1988.

(11) Pohl, W., M.J. v.d. Hoek, J.P. Buis, C.J.L. Florie, S.L. Hancock, P.H.L. Groenenboom, D.J.E. Hesselink, H. Lenselink, and P.J.J. Schaffers. The PISCES Software for DEFENSE. The Netherlands. PISCES International, B.V., 1984.

(12) Rogers, William, Chairman, et.al. Report of the Presidential Commission on the Space Shuttle Challenger Accident. Washington, D.C. June, 1986.

(13) Saderholm, C.A. CPIA/M2 Questionnaire, Unit No. 1173 Pages 1-4, TPH-1148. Thiokol Corporation, Wasatch Division, Brigham City, Utah, October, 1979.